Eddies and the General Circulation of an Idealized Oceanic Gyre: A Wind and Thermally Driven Primitive Equation Numerical Experiment

A. R. ROBINSON AND D. E. HARRISON

Center for Earth and Planetary Physics, Harvard University, Cambridge, Mass. 02138

Y. MINTZ AND A. J. SEMTNER[1]

Department of Atmospheric Sciences, University of California, Los Angeles, 90024

(Manuscript received 21 October 1976, in revised form 24 December 1976)

ABSTRACT

We present the results of a multi-level, constant depth, primitive equation general ocean numerical circulation simulation with mesoscale resolution. A single mid-latitude model gyre is driven by wind and heating. After 30 years of spin-up with a relatively coarse grid and large diffusion coefficients, the grid size and diffusion coefficients are reduced. The circulation then adjusts into a nonlinear and time-dependent flow with periods of tens of days and space scales of hundreds of kilometers. After a quasi-equilibrium state is achieved, two years of data are obtained which are separated into time-mean and time-dependent fluctuations, and analyzed. Dynamically distinct regions are identified, momentum, heat and vorticity balances examined, and energy integrals calculated. Statistical measures of significance and of uncertainty are computed where possible. Eddy energy is produced primarily by Reynolds stress work (barotropic instability) on the mean circulation shear in the recirculation and near-field region of the northern current system. Mean fluctuation correlation terms are presented in some regions at order 1 in the mean heat and vorticity balance and can be the leading ageostrophic effect in the mean momentum balance. The flow is non-quasigeostrophic in some parts of the intense boundary currents.

1. Introduction

The general circulation of a model mid-latitude gyre has been studied in terms of a numerical experiment performed with fine horizontal resolution and relatively small constant eddy diffusion coefficients. The model uses primitive equations and has five levels in the vertical. The circulation is forced by a smooth and steady gyre-scale surface wind stress and a surface heat flux based simply on an atmospheric reference temperature linear in latitude. Low-frequency mesoscale motions (eddies) spontaneously appear with energy many times the mean flow energy in the open ocean region of the domain. After an almost statistically steady state is reached, two model years of data are analyzed in order to describe the flow, to examine the mechanism of eddy generation and to explore the effects of the eddies on the mean circulation.

The existence and importance of the low-frequency mesoscale variability of ocean currents has been established in the western North Atlantic by the intensive MODE-1 experiment (e.g., Robinson, 1975; Rossby *et al.*, 1975; McWilliams, 1976). It is now known that the eddy field has considerable variation in properties, and probably dynamics, over the gyre, i.e., it is spatially inhomogeneous (Dantzler, 1977; Schmitz, 1976). Furthermore eddies are known to exist in other oceans (e.g., Bernstein and White, 1974) and may well be ubiquitous (Wyrtki *et al.*, 1976). Little is understood from presently available experimental and observational data about eddy production and the role of eddies in the mean circulation.

Analytical and numerical modeling provide the only direct means of examining detailed questions of dynamics, albeit in idealized circumstances. Much of our current understanding about the dynamics of these motions in the mid-latitudes has come from specialized numerical studies. Holland and Lin (1975) have demonstrated the spontaneous generation of eddies in simple primitive equation, two-layer, β-plane, flat-bottomed, rectangular basins and have examined the qualitative role of the eddies in the overall circulation energetics under variation of several model parameters. Rhines (1975, 1976) and Bretherton and Owens (1976) have examined the quasi-equilibrium behavior of various initial value problems in periodic, β-plane, two-layered or multi-layered, quasi-geostrophic oceans with and without linearized bottom topography in efforts to model the mid-ocean eddy field.

A long-term goal of numerical modeling is to provide a coupled atmospheric/oceanic model capable of dealing with questions of long-term weather forecasting

[1] Present affiliation: National Center for Atmospheric Research, Boulder, Colo. 80303.

and climate dynamics. Such a model requires that the effects of oceanic mesoscale eddies be understood, via eddy resolving models, even if they are later incorporated into the coupled model through parameterization. Of particular importance to the atmospheric model are thermal exchanges between the ocean and the atmosphere which are affected by the thermal transports within the ocean. The eddy field itself may produce significant transports of heat and momentum or may indirectly affect the mean transports of these quantities by influencing the character of the mean flow.

Wind and thermally driven multi-level primitive equation (PE) calculations are an essential component of the effort to construct such a model. They allow the explicit evaluation of eddy and mean thermal processes in the presence of several degrees of freedom in the vertical. They also allow for the possibility of non-quasi-geostrophic flow which may be of physical significance, especially in regions of intense current or strong meandering. Such regions are emerging as significant ones for eddy production and eddy mean field interaction. The models are also consistent with the inclusion of finite-amplitude bottom topography.

Multi-level primitive equation simulations which are time consuming to run must deal with long baroclinic spin-up times. In the high-resolution phase, this experiment requires approximately one hour of IBM 360/91 time per month of data. It is not feasible to perform extensive parametric studies at this time, but it is possible to seek insight from the comparison of a few PE simulations with simpler model results, e.g., quasi-geostrophic two-layer calculations. The multi-level, wind and thermally driven PE calculation reported here is a first effort at beginning such PE modelling in terms of an idealized flat-bottom single gyre. A related second study (Semtner and Mintz, 1977) examines the circulation of a multiple gyre in the presence of continental slope and shelf topography and also with a modified eddy diffusion parameterization.

Section 2 describes the physical model system, the numerical parameters chosen for this calculation, the spin-up and the nature of the quasi-equilibrium state achieved. Section 3 describes qualitative and quantitative aspects of 600-day records of the quasi-equilibrium flow, instantaneous, mean and fluctuations. Section 4 describes the balance of terms for the heat, momentum and vorticity equations and Section 5 presents the results of a basin-integrated energetic analysis. The results are discussed in Section 6.

2. The experiment

a. The model and its parameters

The model basin is approximately a square with side $L=2000$ km in the horizontal plane and uniform depth $H=4$ km. The basin is centered at 35°N latitude. The dynamical boundary conditions are an applied sinusoidal wind stress of amplitude $\tau_0=4$ dyn cm^{-2} on the rigid surface, free slip on all four side walls, and a quadratic drag on the bottom. The thermal boundary conditions are a surface heat flux proportional to the difference between the circulation-dependent sea-surface temperature and a zonally uniform atmosphere reference temperature with prescribed zonally uniform temperature distribution $T_N(Z)$, $T_S(Z)$ on the northern and southern walls and no heat flux through the eastern and western walls and the bottom. Subgrid-scale horizontal diffusion of momentum and heat are parameterized by constant eddy diffusion coefficients $A_M=2\times10^6$, $A_H=7\times10^6$ (cm^2 sec^{-1}) and the vertical diffusion of both quantities by the same constant $K=1.5$ cm^2 s^{-1}.

The choice of these conditions and quantities and some of their implications deserve explanation. Fine horizontal resolution restricts us for practical reasons to a relatively small model domain. The horizontal extent was determined by the need to keep the horizontal grid to 50×50 grid points for computational resource reasons while maintaining approximately 40 km resolution for the high-resolution calculations. The latter scale is roughly the value of the first internal radius of deformation over much of the interior western North Atlantic. The horizontal eddy diffusion coefficients are as small as is computationally feasible for the grid spacing used. The vertical coefficient is not inconsistent with ocean tritium data estimates (Rooth and Ostlund, 1972).

The boundary conditions on the northern and southern walls model the interconnection of the gyre to the rest of the ocean. The dynamical boundary conditions are known to affect the character of the northern boundary current and, as in Holland and Lin (hereafter H&L), we have chosen free slip which tends to allow the current to flow eastward along the boundary latitude (Blandford, 1971). The imposition of temperatures $T_S(Z)$ and $T_N(Z)$ was chosen to allow diffusive heat flux through these walls. This was an attempt to avoid the necessity of a completely closed thermal circulation, including concentrated sinking, from occurring in the model subtropical gyre. Thus all of the boundary heat fluxes in the model are coupled to the circulation and aspects of the thermal forcing can be examined *a posteriori* only.

It is, of course, the nondimensional statement of the model and its parameters which is physically meaningful. Certain nondimensional parameters for this experiment are defined and evaluated in Table 1. The choice of wind stress amplitude affects the value of several factors. The limited east–west extent of our model domain requires that the model wind stress amplitude be 2–3 times greater than a true oceanic value in order to have reasonable transport in the western boundary current. Furthermore, r_W and r_N are measures of the ratio of diffusive and inertial processes in the western and northern boundary layers. For this

TABLE 1. Eddy resolving numerical experiments.

Case	$R_0(\times10^{-4})$	$E_K(\times10^{-5})$	r_W	r_N
This study	1.2	0.1	1.9	1.3
H&L 1	2.2	1.7	3.4	2.0
H&L 2	2.2	10.2	6.7	3.4
H&L 3	2.2	0.5	2.3	1.5
H&L 4	4.8	1.7	2.3	1.6
H&L 5	2.2	1.7	3.4	2.0
H&L 7	0.3	0.2	5.0	2.4

$R_0=\tau_0/(\beta^2L^3H_1)$ $\quad W_F=2(A_m/\beta)^{\frac{1}{3}}$

$E_K=A_m/(\beta L^3)$ $\quad W_I=(\tau_0/(H_1\beta^2L)^{\frac{1}{3}}$

$r_W=W_F/W_I$ $\quad W_F^N=2(A_mL/\beta)^{\frac{1}{3}}$

$r_N=W_F^N/W_I^N$ $\quad W_I^N=(\tau_0/H_1\beta^2)^{\frac{1}{3}}$

In the above A_m is the lateral momentum diffusion coefficient, τ_0 the wind stress normalized by ρ_0, L the basin dimension, H_1 a thermocline depth (10^5 cm in all cases), and β is $2\Omega\cos\varphi_0/a=2\times10^{-13}$ cm^{-1} s^{-1}.

system the amplitude τ_0 must be about 4 dyn cm^{-2} if diffusive and inertial processes are to be of comparable importance ($r_N\approx1$) in the northern boundary current system. As the northern boundary current system was expected to be an important region for eddy-mean field interaction (H&L), the above value was adopted. The A_m value used corresponds to linear boundary layer widths that are marginally resolved with our grid.

Table 1 also presents for comparison purposes parameters for several of the experiments of H&L. The present experiment has the highest Reynolds number (R_0/E_K) of the tabulated experiments; it is relatively less viscous and more inertial. Table 1 will be of interest in the comparison of our results with H&L given in Section 6.

The present computation is to the best of our knowledge the first PE combined wind and thermally driven eddy resolving model gyre experiment. To place it in context with respect to previous model gyre experiments with coarser resolution we list here parameters corresponding to those used in the summary and review by Bryan (1975, Table 2):

$$\left.\begin{aligned} R_0=v^*/(2\Omega La)=8\times10^{-6},\quad E_k=A_m/(2\Omega a^2)=3\times10^{-7}\\ \mathrm{Re}=v^*a/A_m=260\\ P_e=v^*a/A_H=73,\quad \gamma=v^{**}/v^*=11 \end{aligned}\right\}.$$

Here

$$v^{**}=\tau^*/(2\Omega\rho_0D),\quad v^*=(g\Delta\rho/2\Omega)(K/a)^{\frac{1}{3}},$$
$$D=(Ka/v^*)^{\frac{1}{3}},$$

τ^* is the wind stress curl amplitude and $\Delta\rho$ the imposed north–south surface density difference. The parameter γ, which describes the relative importance of wind and thermal driving in model systems with diffusive-advective thermocline balance, is probably not relevant here because our heat balance will be seen to be primarily advective.

b. Equations of the model

The equations chosen to describe the model physics are a slightly modified form of the traditional primitive equations (Bryan and Cox, 1968):

$$\frac{\partial u}{\partial t}+L(u)-\frac{uv\tan\varphi}{a}-fv=-\frac{1}{\rho_0a\cos\varphi}\frac{\partial p}{\partial\lambda}+K\frac{\partial^2u}{\partial z^2}+A_m\nabla_H^2u, \quad (2.1)$$

$$\frac{\partial v}{\partial t}+L(v)+\frac{u^2\tan\varphi}{a}+fu=-\frac{1}{\rho_0a}\frac{\partial p}{\partial\varphi}+K\frac{\partial^2v}{\partial z^2}+A_m\nabla_H^2v, \quad (2.2)$$

$$0=-\frac{\partial p}{\partial z}-pg, \quad (2.3)$$

$$\frac{\partial T}{\partial t}+L(T)=\frac{K}{\delta}\frac{\partial^2T}{\partial z^2}+A_H\nabla_H^2T, \quad (2.4)$$

$$\frac{1}{a\cos\varphi}\left[\frac{\partial u}{\partial\lambda}+\frac{\partial}{\partial\varphi}(v\cos\varphi)\right]+\frac{\partial w}{\partial z}=0, \quad (2.5)$$

where a is the radius of earth, $(\lambda,\varphi,z)=$ (longitude, latitude, depth), and

$$L(\sigma)=\frac{1}{a\cos\varphi}\left[\frac{\partial}{\partial\lambda}(u\sigma)+\frac{\partial}{\partial\varphi}(v\sigma\cos\varphi)\right]+\frac{\partial}{\partial z}(w\sigma),$$

$$f=2\Omega\sin\varphi,$$

$$\delta=\begin{cases}0, & \text{if } \dfrac{\partial T}{\partial z}<0\\ 1, & \text{otherwise}\end{cases}$$

$$\nabla_H^2\sigma=\frac{1}{a^2\cos^2\varphi}\frac{\partial^2\sigma}{\partial\lambda^2}+\frac{1}{a\cos\varphi}\frac{\partial}{\partial\varphi}\left(\cos\varphi\frac{\partial\sigma}{\partial\varphi}\right),$$

$$\rho=\rho_0[1-\alpha(T-T_0)].$$

Spherical terms in momentum diffusion have been dropped because of the limited basin extent; the domain spans 18° of latitude (southern boundary at 26°N) and 22° of longitude.

The surface wind stress has the form

$$\tau(\varphi)=\tau_0\cos\pi\left[\frac{\varphi-\varphi_N}{\varphi_N-\varphi_S}\right], \quad (2.6)$$

where φ_N, φ_S are the northern and southern latitudes of the basin boundaries. The surface heat flux is com-

puted from (see Haney, 1971)

$$K\frac{\partial T}{\partial z}\bigg|_{z=0} = Q_0(T^*-T_1), \tag{2.7}$$

where T_1 is the model upper level temperature and $T^*=T^*(\varphi)=26-(7/9)(\varphi-\varphi_S)$ [°C] and $Q_0=60$ cm day^{-1}. At the bottom, we use the quadratic drag law of Weatherly (1972)

$$\left.\begin{aligned} K\frac{\partial u}{\partial z}\bigg|_{z=-H} &= \rho_0 C_0(u_L^2+v_L^2)^{\frac{1}{2}}(u_L\cos\Delta - v_L\sin\Delta) \\ K\frac{\partial v}{\partial z}\bigg|_{z=-H} &= \rho_0 C_0(u_L^2+v_L^2)^{\frac{1}{2}}(v_L\cos\Delta + u_L\sin\Delta) \end{aligned}\right\}, \tag{2.8}$$

where $C_0=(0.035)^2$, $\rho_0=1$ g cm^{-3}, u_L and v_L are the model deep water velocities and $\Delta=10°$ is an inflow angle. $T_N(Z)$ and $T_S(Z)$ were determined by zonally averaging the results of a larger scale viscous experiment (Haney, 1974); the results are 10.7, 10.6, 9.3, 7.0, 4.1°C for $T_N(Z)$ and 24.4, 19.8, 11.7, 6.2, 4.3°C for $T_S(Z)$ at the temperature grid point depths given below.

c. *The numerical model*

The domain is discretized into a staggered grid with spacing 0.36° in latitude and 0.44° in longitude between like grid points (~40 km). Five levels in the vertical for the u, v, T calculations were chosen in order to provide surface, near surface, upper thermocline, lower thermocline and deep water levels. Temperature, pressure and transport streamfunction are defined on a normal integer grid: (i,j,k) $i=1, 51$; $j=1, 51$; $k=1, 5$, (no vertical dependence for transport streamfunction), and the lateral extreme points lie on the physcial boundary of the domain. Vertical levels are 40, 160, 490, 1130 and 2690 m. Horizontal velocity (u,v) is computed at half-integer grid points in the horizontal, but at the same depths as T, P, ψ: $(i+\frac{1}{2}; j+\frac{1}{2}, k)$ $i=1, 50$; $j=1, 50$; $k=1, 5$. Vertical velocity is computed at half-integer points overlying the temperature grid $(i, j, k+\frac{1}{2})$ $i=1, 51$; $j=1, 51$; $k=1, 4$, and then is four-point horizontally interpolated for vertical advection of horizontal velocities. Vertical levels are 100, 325, 900 and 2000 m. See Fig. 1 for a picture of the grid box structure.

The numerical model is formulated as in Semtner and Mintz (1977), except that temperatures are imposed external to the northern and southern boundaries. These temperatures influence the circulation-dependent diffusive heat fluxes across these boundaries. The heat flux through the boundary is based on a centered difference between the imposed exterior temperature and the first temperature value inside the domain, rather than on a one-side difference between the exterior and boundary temperatures. This situation results from a minor error in the computational program. As the only

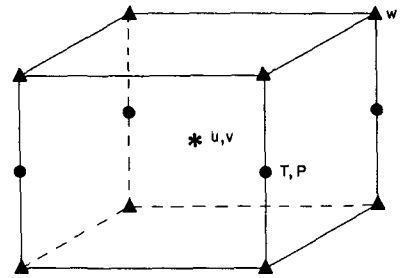

FIG. 1. Schematic drawing of grid point arrangement of the staggered grid.

purpose of imposing these temperatures is to permit the circulation to exchange heat through the boundaries rather than be forced into strong downwelling in the northeast, and since diffusion is found not be be dominant in the heat balance near these boundaries, it is felt that the model physics is not seriously affected. However, the formulation may lead to an increase in computational noise near the boundary.

d. *Spin-up and quasi-equilibrium*

One of the goals of this work is to produce a sufficiently statistically steady circulation so that it is physically sensible to separate the flow into a time mean and a fluctuation part, and to study the effects of the mean eddy terms on the mean flow.

For the initial spin-up phase of the calculation, horizontal resolution of about 100 km and lateral diffusion coefficients $A_m=10^7$ cm^2 s^{-1}, $A_H=10^7$ cm^2 s^{-1} for momentum and heat were chosen in order to allow reasonably quick accumulation of model years for each hour of computer time expanded. The grid size was then reduced to ~40 km and the diffusion parameters reduced. Other changes were made for computational reasons so that the spin-up was a series of initial value problems. For example, the change to the final value of $A_H=7\times10^6$ cm^2 s^{-1} from a previous value of 5×10^6 led to vigorous readjustment in the southwest region of the domain for ~3 years.

In a baroclinic system there are many internal time scales of adjustment of the flow and it is necessary to monitor basin potential and kinetic energy and time series of velocity and temperature to examine trends. After ~30 years of coarse grid spin-up, ~17 years in the high-resolution phase, and ~3½ years beyond the last parameter change, the computed flow is close to what we shall call quasi-equilibrium. The circulation in the last 618 days shows no gross trends in either basin-integrated kinetic energy or potential energy. Fig. 2 shows total kinetic energy as a function of time over 450 days. The potential energy changes by about 0.1% over the last 600 days, corresponding to a net warming of ~0.01°C of the fluid.

Due to the long time scale for baroclinic adjustment of the deep water, the system is not in overall statistical

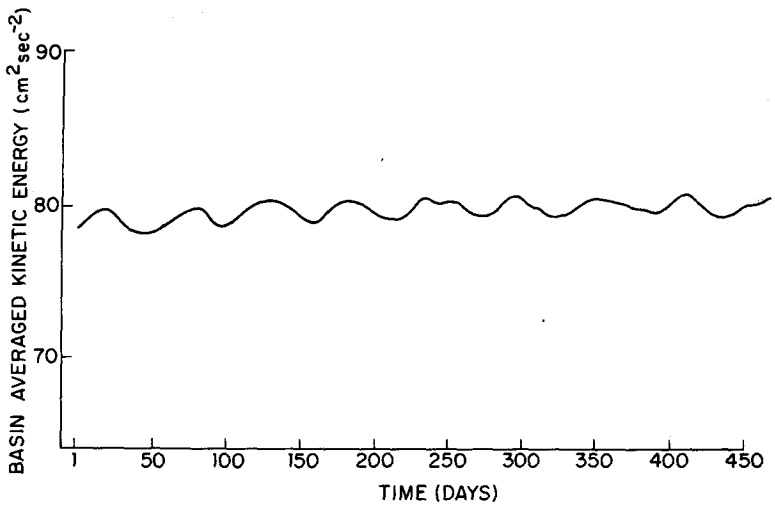

FIG. 2. Time variation of basin-averaged kinetic energy over the first 450 days of the analysis record.

equilibrium. We assume, however, that the slow adjustment of the deep water will not significantly influence the eddy-mean field processes of interest in this study. In none of our sample velocity time-series is there any evidence of trend compared to the eddy signal. Time-series from the upper thermocline and shallower levels in the interior reveal that the eddy signal dominates any trend (Fig. 3a). However, a temperature time-series from the interior at the deepest level shows that the long-term trend can be greater than the eddy temperature signal (Fig. 3b) at depth.

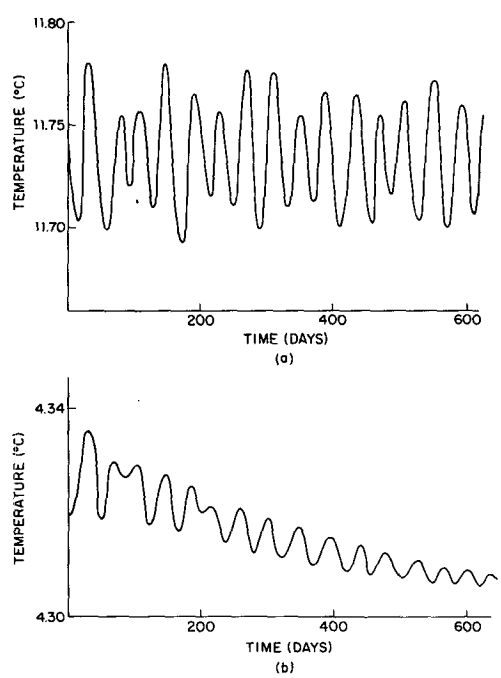

FIG. 3. Temperature time-series (schematic) at two points in the interior of the basin: (a) at the upper thermocline level, 490 m; (b) at the deepest level, 2690 m. (See text.)

The actual temperature fluctuation signal (instantaneous minus mean) is regarded as the sum of a long-term trend plus the signal associated with the mesoscale motions in the domain. We make the working assumption that by removing the trend and computing mean correlation products involving T' (e.g., $\overline{u'T'}$) from the residual fluctuation signal, we can study the mean mesoscale eddy effects in the mean heat equation. The usefulness of this approach for the deep water can be evaluated *a posteriori*.

3. The quasi-equilibrium flow

The first task in understanding a complex three-dimensional time-dependent flow is to describe its characteristics in as simple a fashion as possible. In this section the instantaneous quasi-equilibrium circulation, its time mean and the fluctuation flow (instantaneous minus mean) are described in terms of their distinct regions and scales.

a. The instantaneous flow

Transport streamfunction maps portray the gross characteristics of the horizontal pattern of the quasi-equilibrium flow field. Fig. 4 shows a sequence of maps taken 10 days apart. The boundaries, on which $\psi=0$, are omitted; these are one grid interval beyond the margin in the figure. This was done to avoid congestion of streamlines near the figure margins. The dominant features are described below, followed by the labels that will be used hereafter to refer to the regions associated with these features:

i. A western boundary current of $\sim 60\times 10^6$ m^3 s^{-1} maximum transport (WBC).
ii. A northern wall boundary current of $\sim 180\times 10^6$ m^3 s^{-1} maximum transport, flowing to the east [NBC(E)].

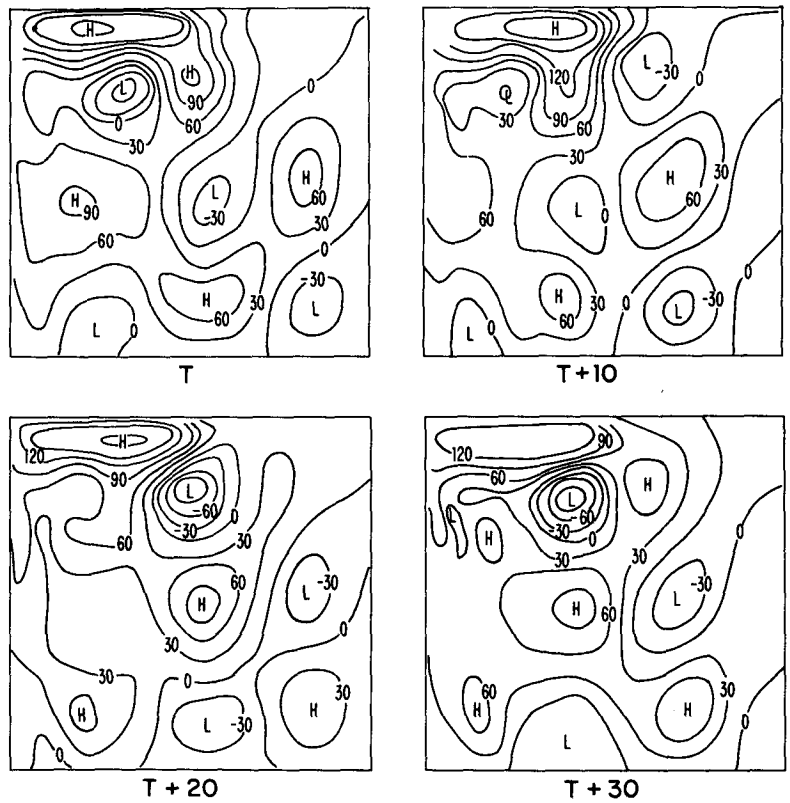

FIG. 4. Contour maps of instantaneous transport streamfunction taken 10 days apart. The boundary condition on ψ is $\psi = 0$ and these grid points are not shown in these maps. All open streamlines close between the northern boundary current system and the actual boundary (see text). Contour interval is 30×10^6 m^3 s^{-1}.

iii. A highly variable northern boundary current recirculation system flowing predominantly to the west [NBC(W)/Near Field].
iv. A mid-ocean circulation dominated by closed circulation systems of $\sim 60 \times 10^6$ m^3 s^{-1} maximum transport that propagate to the west and appear to be periodic with periods of ~ 40 days (Interior).

The visual spatial inhomogeneity of this flow suggests that there will be different physics associated with these regions. Examination of the balance of terms (Section 4) reveals that this is in fact the situation, and so the descriptions that follow will be based upon the behavior of the flow in these regions.

A similar series of pressure and temperature maps yields information about the baroclinic characteristics of the flow. Upper thermocline depth (490 m) temperature maps reveal strong temperature gradients along the northern and western walls, corresponding to the NBC(E) and WBC observed in the streamfunction maps. Typically there is 2°C temperature change between the boundary temperature grid point and its interior neighbor in the WBC and there is between 1.5° and 3.0°C change in the NBC(E). There is no temperature structure in the NBC(W) region, except for the eddy temperature signal which consists of closed temperature anomalies of ~ 1°C at 490 m that propagate to the west at ~ 25 cm s^{-1} as is observed from the streamfunction maps. In the Interior at this depth, the eddy field is visible as modulation of the isotherms rather than as closed contours (with 0.5°C as the contour interval).

Time-series of temperature at various points reveal that the peak-to-peak temperature signals as a function of depth and region can be summarized as follows:

i. O(1°C) at levels 1, 2, 3; O(0.1°C) at levels 4, 5 in the NBC(W)/Near Field.
ii. O(0.5°C) at levels 1, 2, 3; O(0.05°C) at levels 4, 5 in the NBC(E).
iii. O(0.2°C) at levels 1, 2, 3; O(0.01°C) at levels 4, 5 in the Interior and the WBC region.

Temperature signals in the Southwest can be marginally larger (factor of 2) than in the Interior.

The pressure maps at 490 m give a qualitatively similar picture to that obtained from the temperature maps: closed contours appear in the NBC recirculation region and only modulation of the Interior isobaths is seen. However, the eddy pressure signal remains relatively constant with depth so that the closed NBC recirculation eddies are quite evident at 1310 and 2690

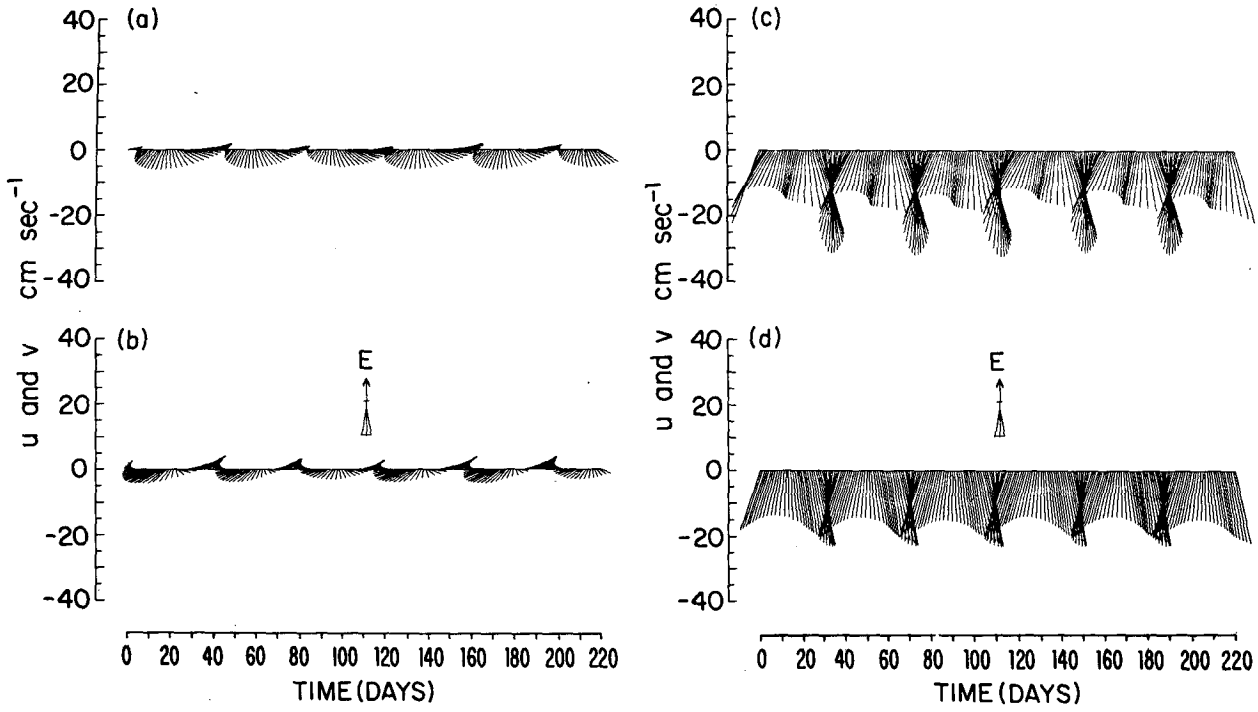

FIG. 5. Time series of (u,v) over the last 220 days of the analysis record at four points: (a) Interior, upper thermocline (490 m); (b) Interior, deep water (2690 m); (c) NBC(W)/Near Field, upper thermocline; (d) NBC(W)/Near Field, deep water. Note the periodic nature of the eddy flow, the presence of shorter period motion in (c) and the barotropic character of the interior flow.

m while in the Interior isobath modulation is quite strong.

Time-series of (u,v) at various points yield the following summary of peak-to-peak velocity data as a function of depth and region:

i. $\sim$25 cm s^{-1} at levels 1, 2, 3; $\sim$15 cm s^{-1} at levels 4, 5 in the NBC(W)/Near Field.
ii. $\sim$15 cm s^{-1} at levels 1, 2, 3; $\sim$7 cm s^{-1} at levels 4, 5 in the NBC(E).
iii. $\sim$20 cm s^{-1} at all levels in the Interior and the WBC region.

There is evidence for bottom intensification of the signal from 15 cm s^{-1} at levels 1, 2, 3 to 20 cm s^{-1} deep in the southwest corner of the domain.

A (u,v) versus time stick diagram (vector time series) is drawn for several points in Fig. 5 and illustrates the periodicity that exists at all levels and in all regions of this flow. To determine the sampling interval for the time series of data to be analyzed, time series of data sampled every time step (30 min) were first searched for high-frequency motions. The highest frequency at which any energy was found has a period of about 10 days. Thus one day sampling was selected to give adequate resolution and to avoid aliasing errors.

Sample periodograms for velocity spectra were computed at a number of sample points in order to examine the distribution of eddy energy as a function of frequency. Fig. 6 shows sample periodograms for zonal velocity at Interior and NBC recirculation thermocline points. In the Interior the dominant period is about 40 days with some evidence for a weaker 60-day motion. A more complicated situation is found in the NBC recirculation system where considerable energy is found at periods of about 40 and 20 days, but weaker energy levels are also evident at about 60 days and at several high frequencies. Spectral analysis has not been done to examine the significance of the secondary time scale motions and is unnecessary for the dominant 40-day motion. The higher frequency motions are only found in the upper three levels of the ocean in the NBC recirculation and WBC regions.

Table 2 summarizes the scales of the instantaneous fields at two depths and includes space scale estimates based upon velocity maps. Root-mean-square as well as peak-to-peak sample amplitudes are presented. Note that there is no space scale variation with depth in any region of the flow.

b. Stability, significance and uncertainty of means

Before describing the mean properties of the circulation, a few remarks about computing and evaluating time means are necessary. Because the computer generates a complete set of physical variables at each time step, it is possible formally to average over any number of time steps and obtain mean and fluctuation fields. Whether these fields are appropriate to a physical

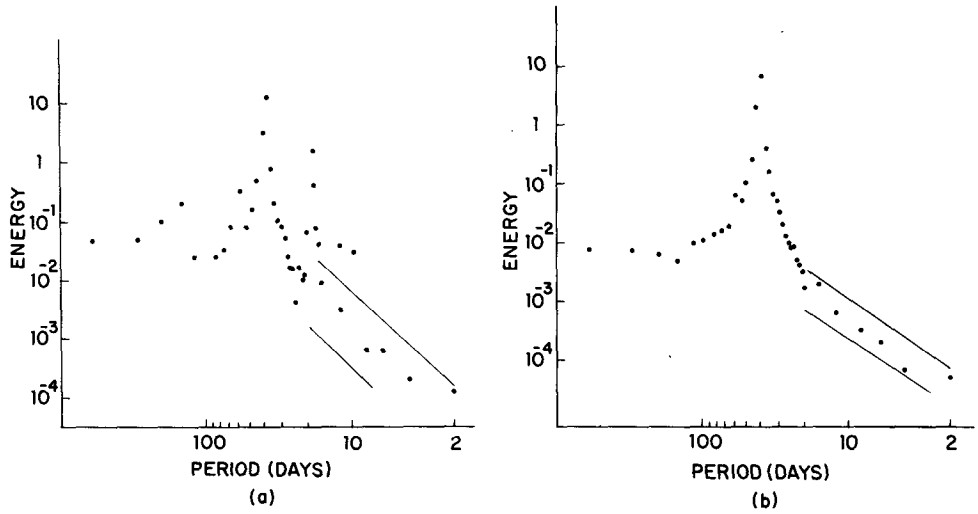

FIG. 6. Sample periodograms of zonal velocity in the upper thermocline (490 m): (a) in the NBC(W)/Near Field and (b) in the Interior. Energy is plotted for all periods longer than 20 days and the parallel lines define an envelope within which all higher frequency points lie (except the two frequency points plotted in (a) which are outside their envelope.

discussion of the time-dependent flow based upon the concept of a time-independent mean flow plus a time-dependent fluctuation flow depends upon several things: the data at individual points must not show significant trend, the point means must be insensitive to the addition of further data (i.e., making the time series longer), and the statistical significance of the means must be established by error estimates.

We have examined time-series of all fields at sample points for trends. As remarked before, the velocity time-series seem to be devoid of trend comparable to the eddy signal while the temperature field is satisfactory in the upper three levels, but can have trend over the record comparable to the eddy signal [O(10^{-2} °C)] in the deeper levels.

The behavior of the point mean values is examined by plotting the mean values as a function of the averaging interval from one to 618 days (Fig. 7). In particular, the largest and smallest mean values found as the averaging interval is increased from 500 to 618 days are differ-

TABLE 2. Regional eddy scales.

Region*	Dominant scale(s) Wavelength (km)	Period (days)	Secondary time scales	Velocity (cm s^{-1}) (rms)	(sample peak-to-peak)	Amplitudes Temperature (sample peak-to-peak)	(standard deviation)
Interior							
Shallow	1400	40	60	4–7	20	0.05°	0.1°
Deep	1400	40	60	4–7	20	0.01°	10^{-3} or less
NBC(E)							
Shallow	1400	40, 60	30, 25, 20, 13	3–5	15	0.5°	0.1°
Deep	1400	40, 60	20	1–3	7	0.02°	0.05 on boundary, otherwise 10^{-3}° or less
NBC(W)/Near Field							
Shallow	600	40, 20	130, 60, 13	9–17	25	1.0°	0.2° –0.3°
Deep	600	40	20, 13	8–15	15	0.2°	0.03°–0.1°
WBC							
Shallow	500	40, 30	130, 60, 25, 20	2–5	20	0.05°	0.1°
Deep	500	40, 30	130, 60	2–4	15	0.01°	0.05° in northeast otherwise 10^{-3}° or less
SW							
Shallow	400	40, 60	130, 25	2–6	15	0.1°	0.1°
Deep	400	40, 60	130, 25	2–7	20	0.05°	10^{-3}° or less

* Shallow, 490m; deep, 2690m.

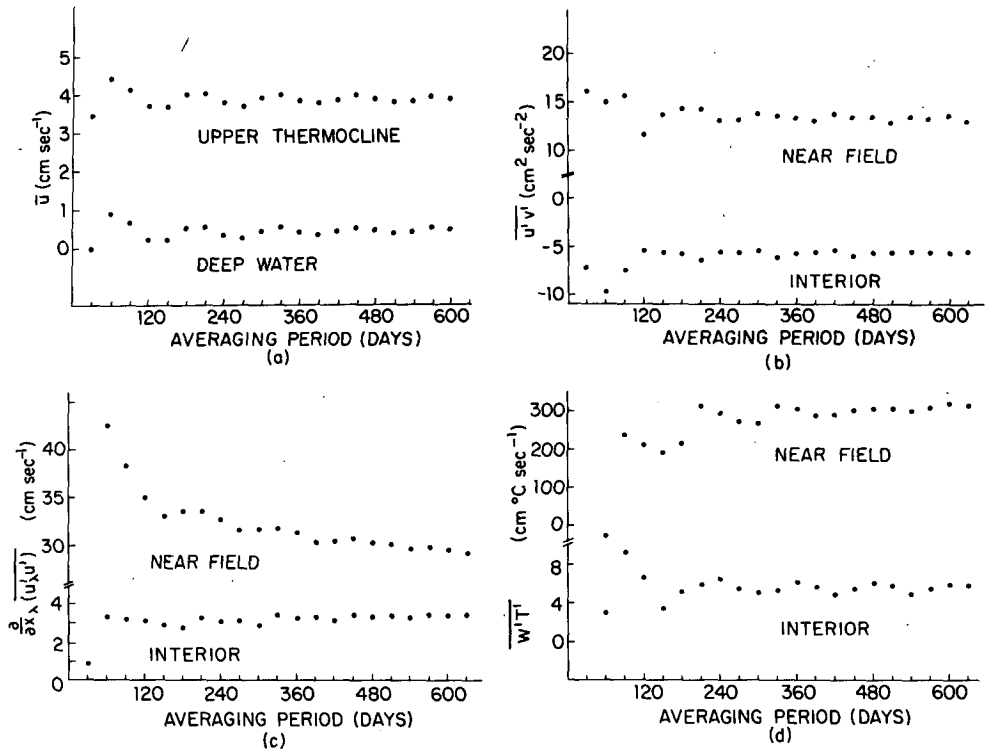

FIG. 7. Sample means and moments versus averaging period: (a) interior mean zonal velocity in the upper thermocline and deep water; (b), (c) and (d) upper thermocline level interior and NBC(W)/Near Field values of $\overline{u'v'}$, $(\partial/\partial_\lambda)\overline{u'_\lambda u'}$ and $\overline{W'T'}$.

enced and expressed as a percentage of the final mean value. This percentage is used as a measure of the stability of the final (618 day) mean values.

For horizontal velocities >2 cm s^{-1} the means appear stable to 5%, in the interval 1–2 cm s^{-1} they are stable to $\sim$15%, and they are not stable for velocities on the order of 1 cm s^{-1} or smaller. Mean vertical velocities are stable to about 5%. Mean temperatures are quite stable, $\sim$1%. Standard deviations for velocity components are stable to about 5%, and temperature standard deviation is similar for levels 1, 2, 3. For levels 4 and 5 (1310 and 2690 m) the eddy signal and trend combine to make the temperature standard deviations unreliable.

In addition to primary field variables and their variances, it is necessary to examine the stability of correlation terms like $\overline{u'v'}$ and $\overline{u'T'}$ and their derivatives. Fig. 7 also displays $\overline{u'v'}$, $(\partial/\partial x_\lambda)(\overline{u'_\lambda u'})$ and $\overline{w'T'}$ as a function of averaging interval.[2] All calculations involving moments of T' are computed from temperature time-series with the trend removed. They are stable to order 20% but some still show a small trend at the end of the analysis record. Increased record length would be necessary if accurate quantitative examination of interrelationships of mean to eddy physics were sought.

The third criterion, estimation of uncertainty for the means, is not entirely straightforward (Leith, 1973). To have a sample mean and standard deviation is not enough, for there must be an estimate of the number of degrees of freedom in the data in order to compute an error bar. The above means were computed from a 618-day record subsampled daily for primary field means and every third day for correlation means (henceforth, moments). Using a "Student's t" distribution (asymptotically normal for large degrees of freedom), the mean and associated uncertainty are $\bar{\phi} \pm (t_\nu^{(\mu)}/\nu^{\frac{1}{2}})\sigma_{\bar{\phi}}$, where ν is the number of degrees of freedom in the data, $\bar{\phi}$ the sample mean, $\sigma_{\bar{\phi}}$ the sample standard deviation, and $t_\nu^{(\mu)}$ the value of Student's t for ν degrees of freedom appropriate to the confidence level μ.

Using 95% confidence limits and 618 degrees of freedom (assuming as a limiting extreme that each data point is independent) gives an uncertainty of $\pm(1/13)\sigma_{\bar{\phi}}$. As another extreme, using 15 degrees of freedom (the number of periods of the dominant energy containing motion in the analysis time series) gives $\pm\frac{1}{2}\sigma_{\bar{\phi}}$. Subject to the first criterion most means and moments are significantly different from zero at the 95% level, while using the second, most quantities away from the intense current regions are not.

[2] The Cartesian tensor form of terms in the basic equations will be used for convenience, along with the summation convention of sum over the range of repeated subscripts with Latin subscripts ranging over 1, 2, 3 and Greek over 1, 2.

A reasonable choice for number of degrees of freedom for our almost periodic flow lies between these two extremes. Flierl and McWilliams (private communication) have developed an error estimation theory based solely on the frequency spectrum of a field and suggest dominant period divided by π as the interval between independent observations for a single line spectrum. This estimate for the degrees of freedom results in an uncertainty of $\pm(1/7)\sigma_{\bar{\psi}}$. Using this measure of error, mean velocities of O(1 cm s^{-1}) or less are not significantly different from zero. It is interesting to note that there is considerable correspondence between this significance criterion and the simpler stability criterion. In almost every case where the mean is stable it is also significant; where it is not stable, it cannot be distinguished from zero in this analysis.

c. *The time mean flow*

1) MEAN TRANSPORT

Fig. 8 shows the mean streamfunction ($\bar{\psi}$) and its standard deviation $\sigma_{\bar{\psi}}$. The regions referred to in Section 3a stand out clearly in the $\bar{\psi}$ map. Note the regular maxima and minima in the $\sigma_{\bar{\psi}}$ map, indicating the regularity and nearly due west propagation of the interior eddy field. There is twice the standard deviation in the NBC(W)/Near Field as there is in the Interior, while the WBC shows no significant activity at the contours drawn. The mean streamfunction itself is qualitatively similar to nonlinear single-gyre experiments by Veronis (1966) and Holland and Lin (1975). There is a boundary circulation system adjoining the northern wall, in which ~120 of the maximum 180×10^6 m^3 s^{-1} transport lies within a closed boundary gyre of N–S width ~350 km, with ~150 km for the NBC(E) and ~200 km for NBC(W) widths. The WBC has a transport of $\sim60\times10^6$ m^3 s^{-1} across 60–80 km. The NBC(W)/Near Field shows considerable spatial structure. The interior circulation is qualitatively similar to the traditional linear Sverdrup interior.

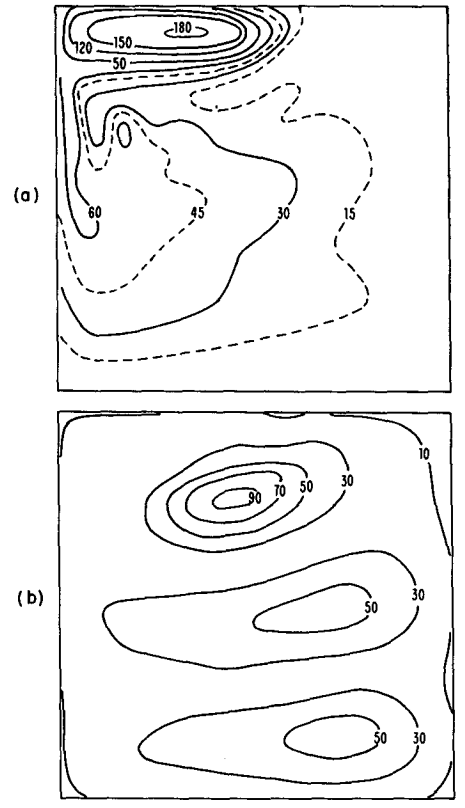

FIG. 8. Mean transport streamfunction $\bar{\psi}$ (a) and standard deviation of $\bar{\psi}$ (b), in 10^6 m^3 s^{-1}; contouring conventions as in Fig. 4.

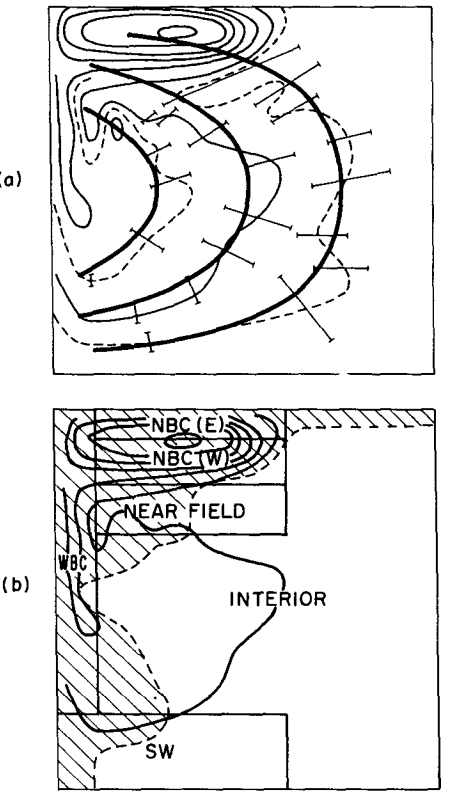

FIG. 9a. Mean transport streamfunction $\bar{\psi}$ plus standard error bars (see text) superimposed on the linear Sverdrup interior solution for the parameters of this experiment. 9b. The dynamical regions of flow superimposed on a map of the basin which shows (cross hatching) where $\bar{\psi}$ departs in a statistically significant way from the Sverdrup interior solution.

Linear transport dynamics and simple scale analysis for this model system predict frictional/inertial western boundary layer widths of ~40 km/~25 km, frictional/inertial northern boundary layer widths of ~180 km/~100 km, and a WBC transport of $\sim60\times10^6$ m^3 s^{-1}. With the exception of the rather larger than predicted WBC width, these theoretical values are close to those observed.

It is of considerable dynamical importance to determine if the eddies have caused any statistically signif-

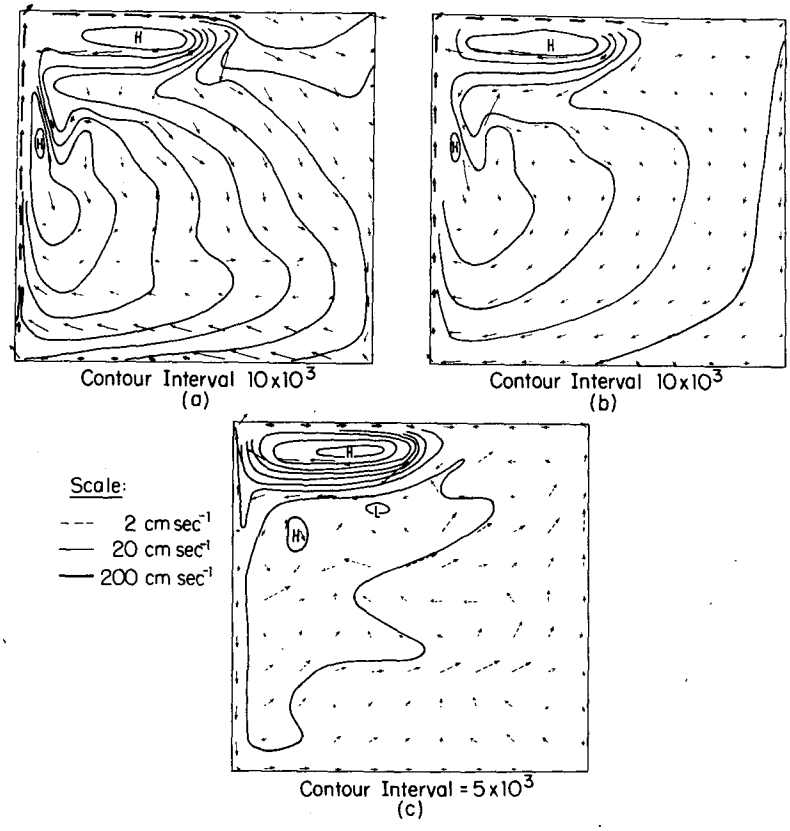

FIG. 10. Mean horizontal velocity $(\bar{u},\bar{v})$ every five grid points superimposed on the mean pressure $\bar{p}$ at (a) 40 m, (b) 490 m and (c) 2690 m. Some $\bar{p}$ contours are partially omitted for visibility of boundary current velocity vectors. $\bar{p}$ units are dyn cm^{-2}.

icant modification of the linear Sverdrup transport in the Interior. Accordingly, error bars (uncertainty as defined in Section 3b) have been calculated for $\bar{\psi}$ and indicated together with the Sverdrup interior streamlines superimposed on $\bar{\psi}$ in Fig. 9a. Fig. 9b shows a schematic figure of the dynamically different regions of the domain and cross hatching is used to indicate the area in which there is significant departure from Sverdrup transport, i.e., where the Sverdrup streamlines do not fall within the envelope of the error bars locally. In the unhatched area of Fig. 9b $\bar{\psi}$ is not statistically significantly different from the Sverdrup solution ψ_s. This unhatched region is composed of the Interior and part of the SW as well as part of the Near Field.

Within the Interior and the southwest the $\bar{\psi}$ field is quite constant as the last few hundred days of data are added. Thus with a longer analysis record, $\bar{\psi}$ might remain as it now is while the error bars would decrease. Where the interior eddy activity is strongest and $\bar{\psi}$ and ψ_s differ by up to 7×10^6 m^3 s^{-1}, smaller error bars would alter the conclusion that $\bar{\psi}$ and ψ_s cannot be satistically distinguished. Where $\bar{\psi}$ and ψ_s are close to one another, the conclusion would not be altered.

The Near Field, on the other hand, can continue to show large variation in $\bar{\psi}$ as the end of the analysis record is reached. However, $\bar{\psi}$ and ψ_s are always different at O(1). Further record length is needed to determine the final structure of $\bar{\psi}$ in this region, but it is plausible to assume that the conclusion with further record length would be that $\bar{\psi}$ is different from ψ_s.

2) MEAN VELOCITY

In this section we present a description of the characteristics of the horizontal flow region by region, and sample values of some of the spatial derivatives needed later for discussion of the instability properties of the mean circulation (Section 6). The mean vertical velocity field is then qualitatively described as a function of depth.

A convenient way to present the overall structure of the horizontal velocity field is shown in Fig. 10, in which mean horizontal velocity vectors are drawn every five grid points (~200 km) and superimposed upon the mean pressure field. This figure shows the high degree of geostrophy in this flow except at the near surface level.

An interior flow field qualitatively similar to the transport field is observed at levels 2, 3 and 4: $\bar{v}$ is negative and a few centimeters per second and $\bar{u}$ shows a minimum at mid-latitude with positive values north and negative values south of this latitude. The surface level flow shows deviation from that of the thermocline levels due to wind driving effects. The weak ($\sim$1 cm s^{-1}) and statistically unreliable interior deep circulation is generally northward in the interior.

The NBC(E) of width $\sim$140 km, has a maximum surface speed of 160 cm s^{-1} at the northernmost grid point 400 km east of the western boundary. It separates from the northern boundary about 1300 km out along the wall, where the maximum speed is $\sim$50 cm s^{-1}. There is considerable vertical shear at the northernmost point but it decreases rapidly southward where the flow is entirely recirculating. The vertical profile of $\bar{u}$ at the point of maximum surface speed is 162, 145, 104, 58 and 37 cm s^{-1}. The maximum value of $\partial^2\bar{u}/\partial y^2$ (computed using the program's second-order differencing) is -8×10^{-12} cm s^{-1} adjacent to the boundary at the surface; a meridional profile of curvature across the NBC(E) 800 km east of the western wall is -5.5, 2.5, 2.0×10^{-12} cm s^{-1}. Typically in the thermocline these values drop by a half.

The NBC(W) of width $\sim$200 km has maximum surface speed located at 900 km east and 250 km south of the northwest corner and a vertical profile of $\bar{u}$ of 39, 35, 27, 21 and 19 cm s^{-1}. At 500 km to the west a more typical profile of $\bar{u}$ is 22, 20, 19, 19 and 18 cm s^{-1}. The flow is quite barotropic shortly after separation and turning, when it has become a westward current. Cross-stream sections of $\partial^2\bar{u}/\partial y^2$ vary with the distance downstream from separation; a surface transect near separation is 1., 0.3, 0.1, -0.1 and -0.1×10^{-12} cm s^{-1} while 500 km downstream values are $O(10^{-14})$ and uniformly positive.

Now consider the WBC region. Maximum velocity is adjacent to the western boundary and $\sim$150 cm s^{-1}; a typical vertical profile of $\bar{v}$ is 137, 130, 98, 35, -3 cm s^{-1}. The width of the boundary current varies from $\sim$120 km in the south to $\sim$50 km further north. There is a deep countercurrent, as the sample above shows, beginning at mid-latitude and with maximum speed of $\sim$10 cm s^{-1}, near the southern boundary.

The overall features of the mean vertical velocity field (not illustrated) are relatively simple. At the bottom of the near surface level (100 m) away from intense currents the classical Ekman divergence vertical velocity field is found. Level 2 (325 m) is similar to level 1 with broad interior downwelling and intense narrow upwelling boundary layers. In the thermocline, level 3 (900 m), there are now regions of interior upwelling and downwelling, but the deep water (2000 m) is pre-

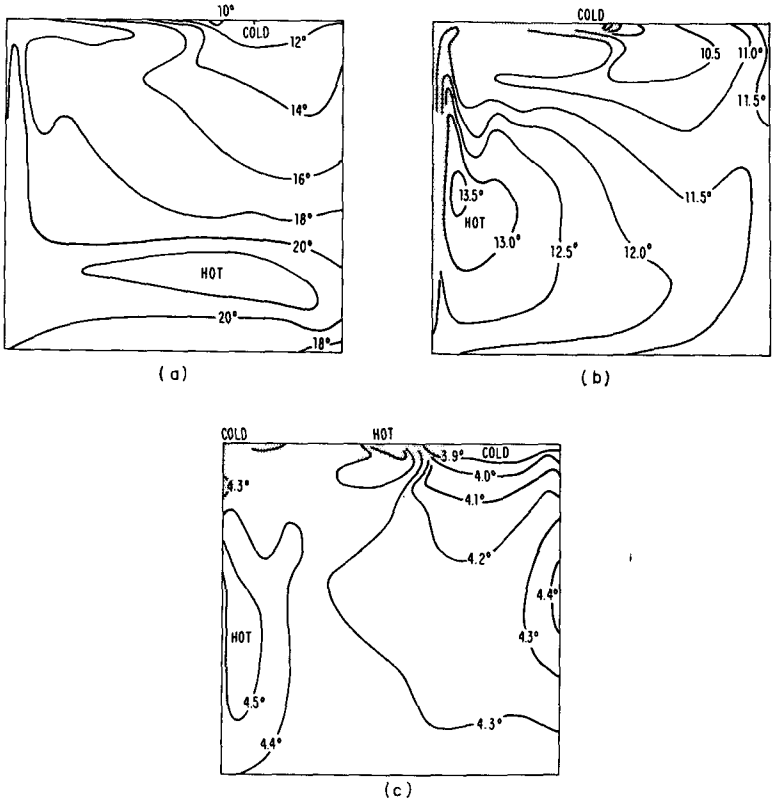

FIG. 11. Mean temperature $\bar{T}$ at (a) 40 m, (b) 490 m, (c) 2690 m. Regions of stippling are discussed in text.

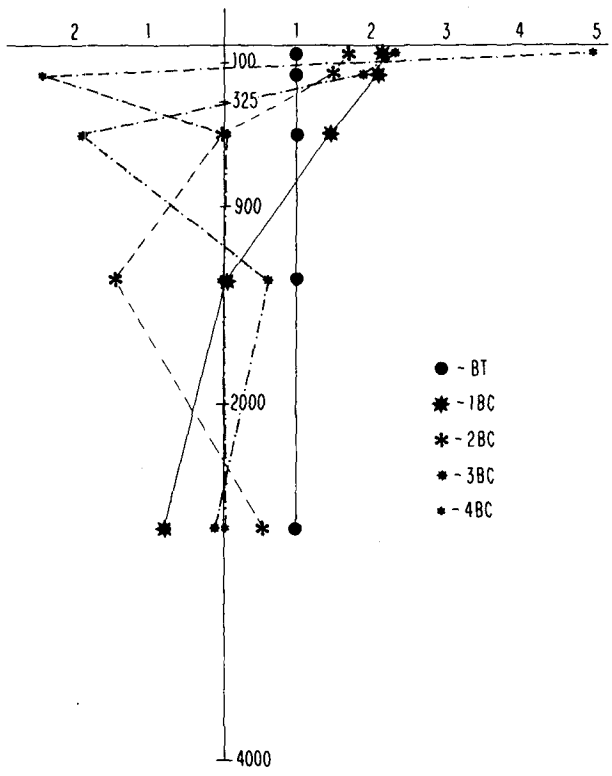

FIG. 12. Normalized horizontal velocity linear quasi-geostrophic eigenfunctions, based upon the horizontally averaged mean temperature field (see text). The value of $F_i(k)$, the ith eigenfunction at level k, is plotted with a spot at the depth of u, v, T grid point for level k and is constant between the labeled depths. Lines are included to aid visualization of the F_i but do not represent the vertical structure of the F_i.

dominantly upwelling. The use of imposed temperatures outside the northern and southern boundaries to permit diffusive heat flux out of the basin in order to avoid a region of intense downwelling in the northeast, as seen, for example, in Bryan and Cox (1968), has been successful. There are nonetheless complex regions of upwelling and downwelling in several parts of the western and northern boundary system currents.

3) MEAN TEMPERATURE

Fig. 11 shows the mean temperature field. At 40 m the field tends toward zonal uniformity with a local maximum about 600 km north of the southern boundary, and with very clold water in the northeast quadrant near the northern wall. The WBC and NBC(E) are clearly visible near the northern and western boundaries.

The upper thermocline level (490 m) field is quite different; the WBC thermal gradient is now comparable to that of the NBC(E), the interior structure resembles $\bar{p}$ at this level, and the coldest water is found somewhat to the west of the NBC(E) separation point from the northern boundary. In the deep water the field shows a tendency toward meridional uniformity. Furthermore the coldest water is found in the northwest corner and in the northeast, and warm water is found near the western boundary, in the NBC(E) separation region, and along the eastern boundary.

As noted in Section 3a, there can be very sharp thermal boundary layers in the thermocline along the northern and western boundaries. In addition to these poorly resolved layers, the 490 and 2690 m $\bar{T}$ maps show some unusual behavior right up against the boundary in the northwest corner and in the separation region of the NBC(E) which is seen as large grid-point-to-grid-point variation in the mean temperature (Fig. 11). These areas cannot be contoured and are indicated by the stippling on Fig. 11.

4) LINEAR VERTICAL MODES

Using the mean stratification data and the numerical model vertical differencing and integration algorithms, it is possible to compute the linear quasi-geostrophic vertical eigenfunctions and eigenvalues (equivalent depths) of the flow (Lighthill, 1969). For horizontally averaged mean temperature data, the equivalent depths are ∞, 1.0, 0.3, 0.2 and 0.02 m corresponding to radii of deformation $(gh_i)^{\frac{1}{2}}/f_0$ of ∞, 38, 21, 17 and 5 km (using f_0 for 35°N latitude). There is only very small variation [O(1) km] in the first baroclinic radius of deformation throughout the basin.

Fig. 12 shows the horizontal velocity eigenfunctions, $F_i(k)$, normalized so that

$$\frac{1}{H}\sum_{k=1}^{5} F_i(k)\Delta z(k)=1.$$

The $F_i(k)$ are a vertically discrete form of the eigenfunctions that are discussed by Lighthill. The solution corresponding to equivalent depth ∞ is the barotropic mode which has uniform amplitude with depth while the higher modes $F_i(k)$ $i>1$, $k=1, 2, \ldots, 5$, are the discrete baroclinic modes of this system. These eigenfunctions provide a convenient, dynamically motivated, means of expanding the vertical structure of the u or v fields in the form

$$\phi(k)=\sum_{i=1}^{5} C_i F_i(k),$$

where k indicates the vertical level and $\phi(k)$ is u or v at level k. Similar expansions have been used in the analysis of oceanographic field data (McWilliams and Flierl, 1976).

Fits of the instantaneous fields suggest that the Interior motion is predominantly barotropic (BT) and first baroclinic (1BC)—80% and 20% of the energy is found, respectively, in these modes. In the southwest quadrant and near-boundary regions the flow is also basically BT plus 1BC but there may be more 1BC energy than BT

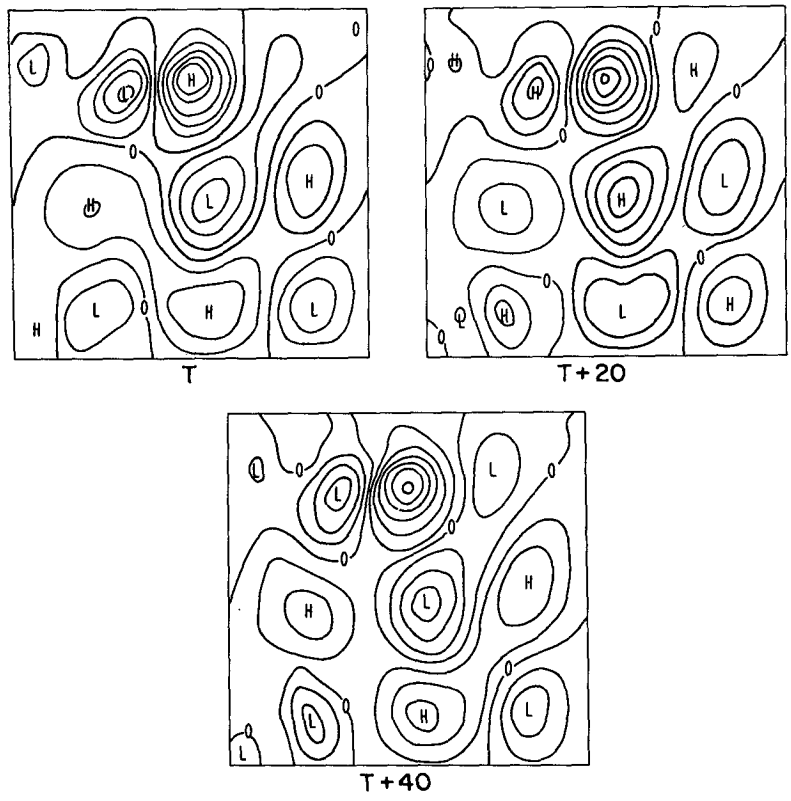

FIG. 13. Eddy transport streamfunction maps ψ' every 20 days beginning with day 200 as in Fig. 4. Contour interval is 20 Sv.

energy. Occasionally energy is observed in 2BC or higher modes at 5–10%, but it is never found systematically throughout a region, and its physical significance is questionable. Lack of horizontal resolution on the scale of the higher internal radii of deformation may restrict the energy content of these modes.

d. The eddy flow and second-order moments

1) THE EDDY FIELDS

A time-series of eddy (instantaneous minus mean) streamfunction maps in Fig. 13 shows that the spatial scale of the barotropic eddy motion is uniform throughout the basin. The flow is quite organized and has two nodal lines at approximately constant latitude. The circulations are similar in some respects to certain free modes of a barotropic β-plane basin. Pedlosky (1965) and Robinson (1965) have described the properties of these free modes and, although no single basin mode exactly accounts for a flow like this eddy field, there are obvious spatial similarities with the (1,3) mode and period similarities with the (1,3) and (2,3) modes. For a square basin of side L, these modes have the form $\exp\{i[(\beta x/2w_{mn})+w_{mn}t]\}\sin(n\pi x/L)\sin(m\pi y/L)$ and the periods of the (1,3) (2,3) and (3,3) modes are 36, 41 and 48 days (for $L=2000$ km) and the corresponding phase speeds of the traveling wave parts ($c=-2w_{mn}^2/\beta$) are 41, 31 and 23 cm s^{-1} to the west. Recall that the dominant period of the eddy circulation is ~40 days and the patterns propagate to the west at ~25 cm s^{-1}.

Maps of the various eddy fields provide a valuable check on the numerical reliability of the calculation; should the eddy field maps be spatially highly variable on a scale smaller than that of the eddy motion either the mean field values are not stable or the calculation is otherwise ill-behaved. Maps of w' reveal small numbers of noisy grid points on the western boundary in the northwest corner and on the northern boundary in the region of NBC separation. There are also areas of noisy w' along the northern and eastern boundaries in the northeast area, extending inward up to three grid points from the boundary. Eddy temperature maps show noisy points in all of these areas except down the eastern boundary. Along the northern and western boundaries they extend up to 3 grid points from the boundary. Because in the northeast this noise does not manifest itself in large enough values of $(\partial/\partial z)(\overline{w'T'})$, $(\partial/\partial z)(\overline{u'w'})$ or $(\partial/\partial z)(\overline{v'w'})$ to play a significant role in the mean field balance of terms, we discount its importance. The NBC separation region and the northwest corner have been seen to be regions of large spatial variation in other fields, and the possibility of significant numerical difficulty cannot be so easily ruled out in these areas.

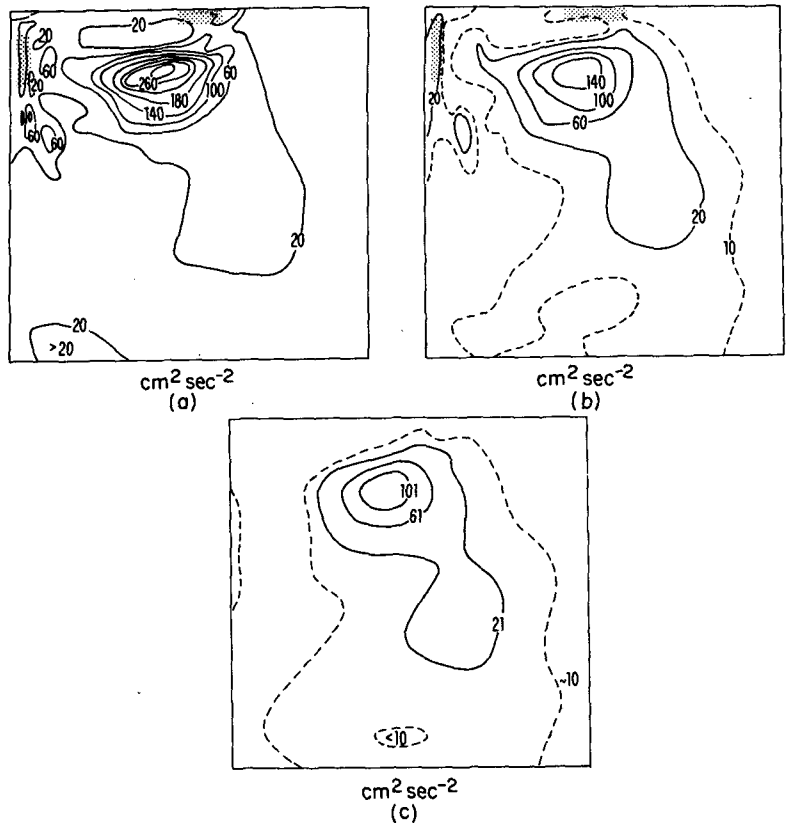

FIG. 14. Mean kinetic energy ($cm^2\ s^{-2}$) of the fluctuations, $\frac{1}{2}(\overline{u'^2}+\overline{v'^2})$ at (a) 40 m, (b) 490 m, (c) 2690 m. Stippled regions have grid-point-to-grid-point variation which cannot be contoured on this scale.

2) SECOND MOMENTS

The mean correlation terms and their derivatives are of considerable physical interest. Fig. 14 shows maps of the mean kinetic energy of the eddy field (MKEF), $\frac{1}{2}(\overline{u'^2}+\overline{v'^2})$, at three levels. At the near-surface level there is a very strong maximum centered on the NBC(W)/Near Field boundary in the east as the current is straightening out after separation and reversal. The maximum value of $\sim 300\ cm^2\ s^{-2}$ drops off over 250 km to the south to a value of $\sim 20\ cm^2\ s^{-2}$ which is typical of the interior. There is considerable sub-eddy-scale spatial variation along the western boundary in the north and in a small region on the northern boundary where the NBC leaves the wall. The other levels show much the same pattern, but with decreasing importance of the variable regions at greater depths. There is little change in MKEF with depth in the interior, while there is a factor of 3 decrease in the Near Field maximum. The mean field interior flow is comparable in magnitude to $(\overline{u'^2}+\overline{v'^2})^{\frac{1}{2}}$ in the thermocline and 5–10 times smaller in the deep water.

We now consider the eddy correlation terms that appear in the mean field equations. It is only through these terms, divergences of mean eddy heat and momentum fluxes, that the eddy fields interact with the mean fields. Both the spatial scales of variation and the magnitude of these terms, relative to other mean equation terms, are of interest. Here we describe the spatial structure of the terms in the upper thermocline (490 m); we will discuss relative magnitudes in Section 4. Schematic maps of the eddy divergence terms are presented in Fig. 15.

Consider the horizontal divergence of the eddy heat flux, $(\partial/\partial x_\lambda)\overline{u'_\lambda T'}$ at 490 m (Fig. 15a). Maximum amplitude is found in the NBC(E) separation region and in the eastern part of the NBC(W), with interior values down by a factor of 10–100. There is considerable eddy-scale spatial variation in the Interior and Near Field; maximum negative values are found at the latitudes of the maximum interior eddy motion while maximum positive values are associated with latitudes of the minimum values. Patterns tend toward zonal uniformity. In the northern part of the WBC and NBC(E) there is spatial variation on sub-eddy scales.

The corresponding eddy term for the $\bar{u}$ momentum equation, $(\partial/\partial x_\lambda)\overline{u'_\lambda u'}$, shows very different spatial structure (Fig. 15c). At 490 m there is little of the tendency toward zonal uniformity observed in the eddy heat flux divergence field; rather this field shows more interior meridional uniformity. Again maximum

amplitudes are observed in the NBC/Near Field system, but with isolated large values in the northern part of the WBC region. In general there is horizontal convergence of $\bar{u}$ momentum by the eddies in the NBC(W), throughout the eastern third of the basin, and in a patch in the south. There is little small-scale spatial variability except along the northern part of the western wall.

The analogous terms for the $\bar{v}$-momentum equation (Fig. 15b) have patterns quite like those of the eddy heat term in their zonal distribution, but the maximum amplitudes are in the NBC(W)/Near Field region and not so close to the boundaries. The spatial variation of this field is on the scale of the eddy fields rather than on that of the mean fields.

Real ocean data are too sparse to permit direct comparison of model data and ocean data eddy divergence terms, but it is possible to compare velocity variances and covariances to Schmitz's (1976) analysis of the available western North Atlantic data. These comparisons are not made in an attempt to verify this particular simulation, but to illustrate the existence of contact points for ocean-model comparisons. Fig. 16 compares meridional cross sections of MKEF at three different longitudes: 4.4°, 8.8° and 13.2° east of the western boundary with North Atlantic data at 55°W and 70°W from Schmitz. The model profiles correspond to longitudes at which the NBC(W)/Near Field is relatively quiet, is quite energetically eddying, and where the NBC(E) separates from the northern boundary. The 70°W profile is quite similar to the 8.8° profile which is taken in the most vigorously eddying part of the NBC system. Comparing profiles of $\overline{u'v'}$ reveals less correspondence between model and ocean data. The 13.2° profile has large positive values south of the NBC system as do the ocean profiles, but the model data values are generally positive through the NBC region while the ocean data are negative, and well south of the jet region the model data take no systematic sign of magnitude while the ocean data are small and positive.

4. Balance of terms

In this section we examine the relative importance of the different terms in the momentum, heat and vorticity equations. It is of interest to ascertain the degree to which the flow is geostrophic, obeys the quasigeostrophic vorticity equation and conserves the quasigeostrophic form of potential vorticity. The role of eddy processes in the mean equations is also con-

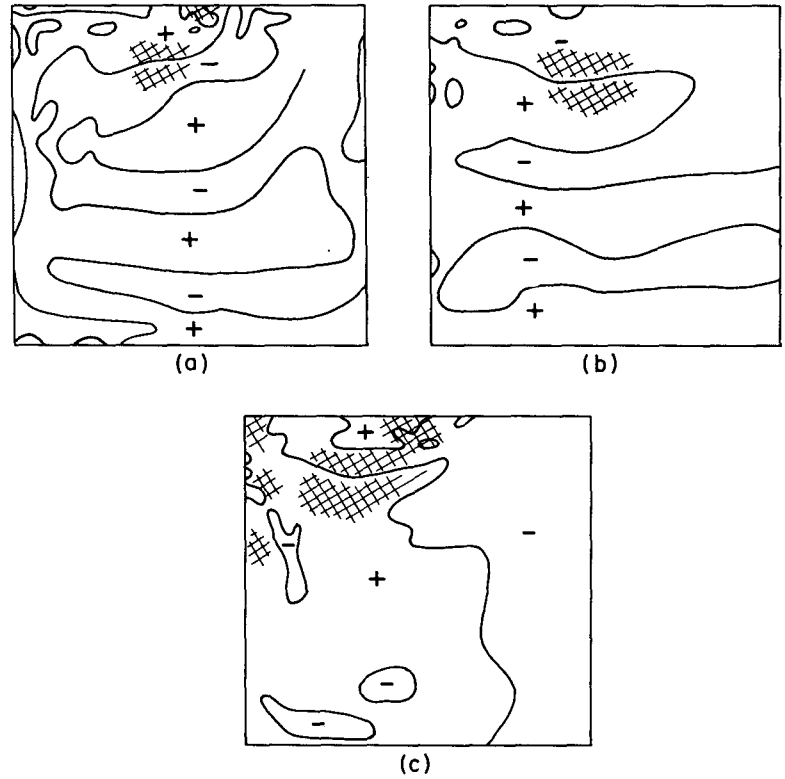

FIG. 15. Schematic features of horizontal divergence of eddy moment terms at the upper thermocline level (490 m): (a) eddy heat flux divergence, $(\partial/\partial x_\lambda)\overline{u_\lambda' T'}$; (b) eddy meridional momentum flux divergence $(\partial/\partial x_\lambda)\overline{u_\lambda' v'}$; (c) eddy zonal momentum flux divergence $(\partial/\partial x_\lambda)\overline{u_\lambda' u'}$. Regions of positive and negative values are shown, with cross hatching to denote the regions of maximum amplitude for each field.

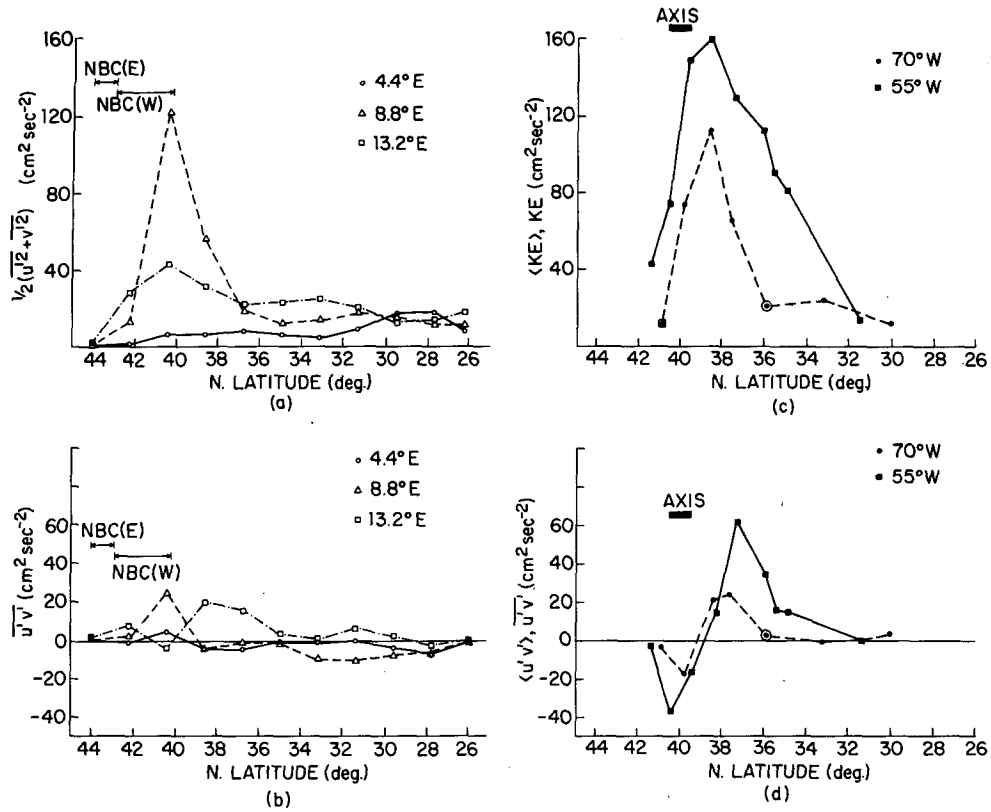

FIG. 16. Comparison of model and ocean: (a) & (c), $\frac{1}{2}(\overline{u'^2}+\overline{v'^2})$ vs. latitude; (b) and (d) $\overline{u'v'}$ vs. latitude. Model data are plotted at three different longitudes, east of the western boundary, with 44°E through a quiet part of the NBC system, 8.8°E through a vigorously eddy-energetic region of the NBC system, and 13.2°E through the separation and turning region of the NBC(E)/NBC(W). Ocean data are at latitudes 70°W and 55°W from Schmitz (1976). (See text.)

sidered, in particular to assess their contribution to the observed deviation from linear Sverdrup transport dynamics and to evaluate their importance relative to constant coefficient diffusions.

A detailed description of relative magnitudes of terms in the different regions of the domain at the upper thermocline level is presented via tables; only substantial departures from the thermocline balances at other levels are noted. The relative magnitudes are referred to the largest term(s) in each region for each equation discussed. Thus the value unity appears at least once in each row of each table, except for the momentum equation where the geostrophic terms are O(1) and are not tabulated. Regional summary generalizations do not always hold at every grid point; for example, intense current regions may show considerable variability of relative magnitudes.

a. Instantaneous balances

We have examined balances for two sample days via a study of detailed discrete contour maps (Harrison, 1977). It is convenient to define the abbreviations:

HA horizontal advection, $u_\lambda(\partial\phi/\partial x_\lambda)$
VA vertical advection, $w(\partial\phi/\partial z)$
HD horizontal diffusion, $A(\partial^2\phi/\partial x_\lambda\partial x_\lambda)$
VD vertical diffusion, $K(\partial^2\phi/\partial z^2)$.
TC time change, $\partial\phi/\partial t$.

Here ϕ is an arbitrary field. TC is computed using forward differences on data one day (48 time steps) apart. Because the time scale of variation is longer than a day, little error is introduced by this procedure.

1) THE HEAT EQUATION (Table 3a)

Note that HA, VA and TC generally enter the O(1) balance, HD is $O(10^{-2}$–$10^{-1})$ relative to them except in the boundary regions where it can be O(1). Time change may be $O(10^{-1})$ in the boundary regions. The term VD is typically $O(10^{-2})$ or smaller but can be O(1) at level 1 and $O(10^{-1})$ at level 5.

2) THE MOMENTUM EQUATIONS (Table 3b)

The instantaneous u-momentum equation (for which no table is presented) is qualitatively similar to the v-momentum equation except in the WBC where it is highly geostrophic and in the NBC(E) where it can show ageostrophic effects at O(1). This is expected from analytical theory—the downstream velocity com-

ponent is quite geostrophic while the cross-stream component shows significant departure from geostrophy. Only in points immediately adjacent to the boundaries (and at level 1 which is wind driven) are ageostrophic effects greater than $O(10^{-1})$.

Note that, for the instantaneous momentum equations, the Interior balance is geostrophic to $O(10^{-2}$–$10^{-3})$, with time change and horizontal advection appearing at that order, with HA generally smaller than TC, and horizontal diffusive effects at $O(10^{-3})$. Vertical and horizontal diffusions are comparable at level 5 and VD is otherwise smaller except through wind driving in the u equation at level 1 where there is $O(1)$ departure from geostrophy. The observed order of ageostrophic effects is consistent with the model circulation interior Rossby numbers of $(2\text{–}5)\times10^{-3}$.

In intense current regions HD and VA can become comparable to TC and HA; VD appears at $O(10^{-1})$ relative to TC at level 5 and is otherwise negligible except at level 1; the downstream components of velocity remain highly geostrophic, but departures at the 10% or greater level are found in the cross-stream component near the wall and at $O(1)$ in the points nearest the wall. Again the order of ageostrophic effects is consistent with traditional dynamical theory for a system with Rossby numbers of about 10^{-2} in the NBC(W)/Near Field and about 10^{-1} in the NBC(E) and WBC. There is spatial variation in the high velocity boundary regions sometimes, in the northwest quadrant often and in the southwest occasionally.

The pressure gradient and Coriolis force terms do not appear in these tables because they are always $O(1)$. The Coriolis term contains both the basic rotation (f_0) and the β-effect (the variation of rotation with latitude). An appropriate measure of the beta effect is $\beta L/f_0$ where L is a typical meridional length scale of the notion and $\beta=2\Omega\cos\varphi_0/a$. For this flow the β-effect is $O(10^{-1})$ in the Interior.

3) VORTICITY

Given the dominant geostrophy of the flow, it is next of interest to inquire into the degree of quasi-geostrophy. For a primitive equation model, the equation for the vertical component of vorticity ζ is

$$\frac{\partial\zeta}{\partial t}+u_j\frac{\partial}{\partial x_j}\zeta-(\zeta+f)\frac{\partial w}{\partial z}+\beta v+\frac{\partial v}{\partial z}\frac{\partial w}{\partial x}-\frac{\partial u}{\partial z}\frac{\partial w}{\partial y}=D_H+D_V,$$

where

$$\zeta=\frac{\partial v}{\partial x}-\frac{\partial u}{\partial y}$$

and D_H and D_V are the curl$_z$ of $A_M\,\partial^2\bar{u}_\lambda/\partial x_\delta\partial x_\delta$ and $K\,\partial^2\bar{u}_\lambda/\partial z^2$. For a quasigeostrophic system with u and v in geostrophic balance to order Rossby number, the vorticity equation reduces to

$$\frac{\partial\zeta}{\partial t}+u_\lambda\frac{\partial}{\partial x_\lambda}\zeta+\beta v-f\frac{\partial w}{\partial z}=0$$

which takes on the form

$$\left(\frac{\partial}{\partial t}+u_\lambda\frac{\partial}{\partial x_\lambda}\right)q=0,\quad q=\zeta+f+\frac{\partial}{\partial z}\left(\frac{f_0^2}{N^2}\frac{\partial p}{\partial z}\right),$$

where $N^2=-(g/\rho_0)(\partial\bar{\rho}/\partial z)$, when the motion is adiabatic and horizontally nondivergent to order Rossby number. The last equation expresses the conservation, following the geostrophic flow, of the quasi-geostrophic potential vorticity q.

Thus, the quasi-geostrophic vorticity equation holds when the relative vorticity is small compared to the planetary vorticity f, when $w(\partial\zeta/\partial z)$ can be neglected compared to $u_\lambda(\partial\zeta/\partial x_\lambda)$, and when the vertical and horizontal momentum diffusion terms are small. Quasi-geostrophic potential vorticity is conserved when the quasi-geostrophic vorticity equation holds and, in addition, diffusive effects in the heat equation can be neglected compared to advection and time rate of change.

Previous balance estimates for heat and momentum involved only terms available from the finite-difference model equations, but not all the requisite vorticity terms are directly available. Expressions consistent with the finite difference form of the momentum equation and with the curl$_z$ operator used to obtain the transport streamfunction equation are used for $\partial\zeta/\partial t$, βv,

TABLE 3a. Instantaneous temperature equation. Relative magnitude of terms at level 3

Region	HA	VA	TC	HD	VD
Interior	1	10^{-1}–1	1	10^{-2}–10^{-1}	10^{-2}
NBC(W)/ Near Field	1	10^{-1}	1	10^{-1}–1	$\leqslant10^{-2}$
NBC (E)	1	10^{-1}–1	10^{-1}–1	10^{-1}–1	$\leqslant10^{-2}$
WBC	10^{-1}–1	1	10^{-1}	1	10^{-2}
SW	10^{-1}–1	10^{-1}–1	1	10^{-1}–1*	10^{-2}–10^{-1}

* Largest on the boundary.

TABLE 3b. Instantaneous v-momentum equation. Relative magnitude of terms at level 3

Region	HA	VA	TC	HD	VD
Interior	10^{-2}	$\leqslant10^{-4}$	10^{-2}	10^{-3}	$\leqslant10^{-5}$
NBC(W)/ Near Field	10^{-2}	$\leqslant10^{-3}$	10^{-2}	10^{-3}	$\leqslant10^{-4}$
NBC(E)	10^{-2}	$\leqslant10^{-2}$	10^{-2}	$\leqslant10^{-2}$	$\leqslant10^{-4}$
WBC*	$\leqslant1$	$\leqslant10^{-1}$	$\leqslant10^{-1}$	$\leqslant10^{-1}$	$\leqslant10^{-4}$
SW	10^{-2}	$\leqslant10^{-4}$	10^{-2}	10^{-3}	$\leqslant10^{-4}$

* Balances vary within the region, considerable magnitude variability of terms.

TABLE 4. Instantaneous vorticity equation.
Relative magnitude of terms at level 3

Region	BV	FWZ	ZWZ	TC	HA	VA	HD	VD	TW
Interior	1	10^{-1}–1	10^{-3}–10^{-2}	1	10^{-2}–10^{-1}	10^{-3}–10^{-2}	10^{-3}–10^{-2}	10^{-5}	10^{-4}
NBC(W)/NF	1	10^{-2}–1	10^{-2}	1	10^{-1}–1	10^{-3}–10^{-2}	10^{-2}–10^{-1}	10^{-4}–10^{-3}	10^{-3}–10^{-2}
NBC(E)	10^{-1}–1	10^{-1}–1	10^{-2}–10^{-1}	10^{-1}–1	1	10^{-2}–10^{-1}	10^{-1}–1*	10^{-3}	10^{-2}–10^{-1}*
WBC	1	10^{-1}	10^{-2}	10^{-2}–10^{-1}	10^{-1}–1	10^{-3}–10^{-2}	10^{-2}–1*	10^{-4}–10^{-3}	10^{-3}–10^{-1}*
SW	1	10^{-1}	10^{-3}–10^{-2}	1	10^{-1}–1	10^{-3}–10^{-2}	10^{-2}–1*	10^{-4}–10^{-3}	10^{-1}–10^{-2}

* Largest near the boundary.

$f(\partial w/\partial z)$, D_H and D_V. Second-order accurate expressions are used for the other terms. Table 4 presents the resultant relative magnitudes. We introduce notation BV, FWZ, ZWZ, TW, HD and VD for the terms

$$\beta v, \quad f\frac{\partial w}{\partial z}, \quad \zeta\frac{\partial w}{\partial z}, \quad \frac{\partial v}{\partial z}\frac{\partial w}{\partial x} - \frac{\partial u}{\partial z}\frac{\partial w}{\partial y}, \quad D_H \text{ and } D_V.$$

The quasigeostrophic vorticity equation holds, to order Rossby number, except 1) adjacent to the boundary in intense current systems where the flow is not geostrophic to order Rossby number and the vortex twisting term $(\partial v/\partial z)(\partial w/\partial x) - (\partial u/\partial z)(\partial w/\partial y)$ cannot be neglected, 2) at the near-surface level where wind driving destroys lowest order geostrophy, and 3) in some parts of the deep water where bottom stress and/or horizontal diffusion are too large. Quasi-geostrophic potential vorticity is not strictly conserved because, as we have shown earlier, diffusion of temperature can seldom be neglected at order Rossby number compared to advection or time rate of change.

b. Mean balances

Having established the order of ageostrophic effects in the instantaneous flow, the most interesting questions in the mean equation balance of terms concern the relative importance of the mean eddy terms compared to mean advection and mean diffusion. In some regions of the basin it is easy to summarize these relationships. but in others there is small-scale spatial variability in some of the mean terms which makes generalization difficult.

As discussed earlier, in regions where the mean flow is weak, the error bars associated with these mean values are comparable to the means. Thus highly differentiated terms like $A_M(\partial^2\bar{u}/\partial x_\lambda \partial x_\lambda)$ must themselves have large error bars in these regions. In principle, propagation of error calculations can be done to assign error bars to the various mean terms, but it is a nontrivial task for a system with this many grid points and terms, especially given the algebraic complexity of the expressions for terms like mean advection. Fortunately in regions of strong mean flow the error bars associated with mean equation terms computed from mean fields are small and the algorithms that are used to compute divergences of mean eddy correlations yield standard deviations for the divergence terms directly. Thus in intense current regions, which we have previously seen are generally regions of maximum eddy effects, the comparison of eddy effects with mean term effects is straightforward. We assume that no serious error will be made in discussing the balance of terms if area average mean magnitude values are used where appropriate.

We introduce the notation HE for the horizontal divergence of an eddy correlation term, e.g., $(\partial/\partial x_\lambda)\overline{u'_\lambda u'}$, and retain the previous notation for terms which are now computed directly from the mean fields. Upon examination the vertical eddy terms were found to be everywhere negligible.

1) THE MEAN HEAT EQUATION (Table 5a)

Eddy effects are greater than or comparable to horizontal diffusive effects over most of the Interior, the Southwest, and the NBC(W)/Near Field in the upper three levels, and are comparable to or less than HD in the deepest two levels. In the NBC(W)/Near Field, horizontal eddy effects enter the O(1) heat balance. Thus the lowest order balance is generally horizontal-vertical advective modified by HE and/or HD. Vertical diffusion is small except at level 1 where surface heating can make it O(1). There is a 1 grid interval boundary layer with VA-HD O(1) balance at the southern boundary. Sub-eddy-scale spatial variation in the HD field is found in the northwestern part of the basin.

2) THE MEAN MOMENTUM EQUATIONS (Tables 5b, 5c)

Table 5c presents the relative magnitudes of the ageostrophic terms of the $\bar{u}$-momentum equation and can be compared directly with Table 5b which gives the $\bar{v}$-momentum terms. Apart from the anticipated differences in the boundary layer regions, the only significant difference is that HE is comparable to HA in the Interior in the $\bar{u}$ equation, but is uniquely the leading ageostrophic term in the $\bar{v}$ equation.

In summary, the dominant momentum balance is geostrophy. Mean horizontal advection (HA) and horizontal eddy effects (HE) are frequently the largest ageostrophic terms and appear at $O(10^{-2})$ except in the boundary current regions where mean horizontal ad-

TABLE 5a. Mean temperature equation.
Relative magnitude of terms at level 3

Region	HA	VA	HE	HD	VD
Interior	1	1	10^{-1}–1	10^{-2}–1	10^{-1}
NBC(W)/ Near Field*	10^{-1}–1	10^{-1}–1	10^{-1}–1	10^{-1}–1	10^{-2}–10^{-1}
NBC(E)	10^{-1}–1	10^{-1}–1	10^{-3}–10^{-2}	10^{-1}–1	10^{-3}–10^{-2}
WBC*	1	10^{-1}–1	10^{-3}–10^{-1}	1	10^{-3}–10^{-1}
SW	10^{-1}–1	10^{-1}–1	10^{-1}–1	10^{-1}–1	10^{-1}

* There is considerable variability in sign and magnitude in the northwest region of the basin.

TABLE 5b. Mean v-momentum equation.
Relative magnitude of terms at level 3

Region	HA	VA	HE	HD	VD
Interior	10^{-4}–10^{-3}	10^{-5}–10^{-4}	10^{-2}	10^{-5}–10^{-4}	10^{-6}
NBC(W)/ Near Field	10^{-3}–10^{-2}	10^{-5}	10^{-3}	10^{-4}–10^{-3}*	10^{-7}
NBC(E)**	10^{-3}	10^{-5}–10^{-3}	10^{-4}	10^{-4}*	10^{-7}
WBC†	10^{-2}–1	10^{-3}–1	10^{-3}	10^{-2}	10^{-6}
SW	10^{-3}–10^{-2}	10^{-5}	10^{-3}	10^{-4}–10^{-3}*	10^{-7}

* Considerable variability.
** At the grid point adjacent to the boundary HA and VA are 10^{-2}.
† At the grid point adjacent to the boundary HA, VA, HD can all be O(1).

TABLE 5c. Mean u-momentum equation.
Relative magnitude of terms at level 3.

Region	HA	VA	HE	HD	VD
Interior	10^{-3}–10^{-2}	10^{-4}–10^{-3}	10^{-3}–10^{-2}	10^{-5}–10^{-3}*	10^{-6}–10^{-5}
NBC(W)/ Near Field	10^{-2}	10^{-5}	10^{-3}–10^{-2}	10^{-3}	10^{-5}
NBC(E)	10^{-1}–1	10^{-3}–1	10^{-3}–10^{-2}	10^{-2}–10^{-1}	10^{-4}–10^{-3}
WBC	10^{-3}	10^{-4}	10^{-4}	10^{-4}–10^{-3}*	10^{-5}
SW	10^{-2}	10^{-4}–10^{-3}	10^{-3}–10^{-2}	10^{-3}–10^{-2}	10^{-5}

* Quite variable.

vection may be generally O(10^{-1}) and at the grid points nearest the boundary, where the flow may be ageostrophic at O(1) due to HA and/or VA and/or HD. In the NBC(W)/Near Field horizontal eddy effects are the leading ageostrophic term in the mean $\bar{v}$-momentum equation. Mean horizontal eddy effects are typically 10 times larger than mean horizontal diffusion (HD), and the latter often shows considerable small scale spatial variation.

3) MEAN VORTICITY; VERTICALLY INTEGRATED (Table 6)

The vertically integrated equation is first discussed in order to compare with classical transport theory and then the thermocline and level-by-level balances are given.

In Table 6 we introduce the notation ED for the curl$_z$ of the eddy momentum terms; all other terms are defined as before but are evaluated using mean field values and then integrated over the basin depth.

In the interior the Sverdrup balance BV and VD (with VD from the curl of the wind stress), holds but it is modified by eddy effects and, close to the Near Field, by horizontal advection, at up to O(1). The Southwest balance is similar, with eddy effects and horizontal advection modifying a basically Sverdrup balance. The WBC balance is almost classical with beta, horizontal advection and horizontal diffusion the dominant balance; adjacent to the boundary twising effects can also enter. BV, VD, HA and ED can all be O(1) in the NBC(W)/Near Field and HD is O(10^{-1}); this is a complex region. The NBC(E) presents an unusual balance in which the curl of the bottom stress enters with horizontal advection at O(1), is modified by beta and horizontal diffusion throughout, and also by vortex twising adjacent to the boundary.

4) MEAN VORTICITY; LEVEL-BY-LEVEL (Table 7)

In order to facilitate comparison with the vertically integrated vorticity balances, discussion is presented region-by-region with variations at different levels noted. There can be considerable horizontal and vertical variation in relative magnitude of terms which enter the basic balances.

In the Interior and the Southwest the dominant balance is β-plane geostrophy, FWZ and BV. Eddy effects modify this balance at O(10^{-1}–1) in the thermo-

TABLE 6. Mean vertically integrated vorticity.
Relative magnitude of terms at level 3

Region	BV	ZWZ	ED	HA	HD	VD	TW
Interior	1	10^{-3}–10^{-4}	10^{-1}–1	10^{-2}–10^{-1}†	10^{-2}–10^{-1}	1	10^{-3}–10^{-4}
NBC(W)/NF	10^{-1}–1	10^{-3}	10^{-1}–1	10^{-1}–1	10^{-1}–1*	10^{-1}–1	10^{-3}
NBC(E)	10^{-1}–1	10^{-3}–10^{-2}	10^{-2}–10^{-1}	1	10^{-1}–1	1††	10^{-2}–1**
WBC	1	10^{-2}	10^{-2}	10^{-1}–1	10^{-1}–1	10^{-2}–10^{-1}	10^{-2}–1**
SW	1	10^{-3}	10^{-1}–1	10^{-1}–1	10^{-1}–1	10^{-1}–1**	10^{-2}–1**

* Spatially variable.
** O(1) only at point adjacent to boundary.
† Can be O(1) to O(10^{-1}) near NF.
†† Through bottom stress.

TABLE 7. Mean vorticity equation.
Relative magnitude of terms at Level 3

Region	BV	FWZ	ZWZ	ED	HA	VA	HD	VD	TW
Interior	1	1	10^{-3}–10^{-2}	10^{-1}	10^{-2}–1	10^{-3}–10^{-2}	10^{-2}–10^{-1}**	10^{-1}	10^{-4}
NBC(W)/NF	10^{-1}–1	10^{-1}–1	10^{-3}–10^{-2}	10^{-1}–1	10^{-1}–1	10^{-3}–10^{-2}	10^{-2}–1*	10^{-4}	10^{-4}–10^{-2}
NBC(E)	10^{-2}–1	10^{-1}–1	10^{-2}–10^{-1}	10^{-2}–10^{-1}	1	10^{-3}–10^{-1}	10^{-2}–1†	10^{-4}–10^{-3}	10^{-3}–1†
WBC	1	10^{-2}–1	10^{-3}–10^{-1}	10^{-3}–10^{-1}	10^{-1}–1	10^{-3}–10^{-1}	10^{-2}–1*	10^{-4}	10^{-4}–10^{-1}†
SW	1	1	10^{-3}	10^{-2}–10^{-1}	10^{-1}–1	10^{-3}–10^{-2}	10^{-2}–1†	10^{-3}	10^{-3}–10^{-1}†

* Spatially variable on sub-eddy scale.
** Largest near Near Field.
† Largest adjacent to lateral boundary.

cline and deep water levels of the Interior, while in the Southwest and upper two levels of the Interior, horizontal advection enters at $O(10^{-1}$–1), and eddy effects are smaller than or comparable to horizontal advection. The curl of the wind stress dominates the surface level balance. Horizontal and vertical diffusion can be $O(10^{-1})$ in the deep water of the southwest near the southern boundary.

The intense current region balances involve more terms and are more variable within each region. In the NBC(W)/Near Field eddy effects, horizontal advection, horizontal diffusion, BV and FWZ can all be O(1) and the relative importance of each changes, as might be expected, depending upon proximity to the separation and turning region, to the downstream part of the NBC(W), or to the Near Field. In the NBC(E), in addition to these processes, vertical advection of relative vorticity and vortex twisting can enter the balance depending upon proximity to the northern boundary and to the separation region. Within the WBC region balances depend upon the distance downstream, the depth and the distance away from the western boundary, but BV, FWZ, horizontal advection, horizontal diffusion, eddy effects, twisting and vertical advection of relative vorticity can all be $O(10^{-1})$ or greater. The variation of relative magnitudes in these balances is a reflection of the current structure in the regions.

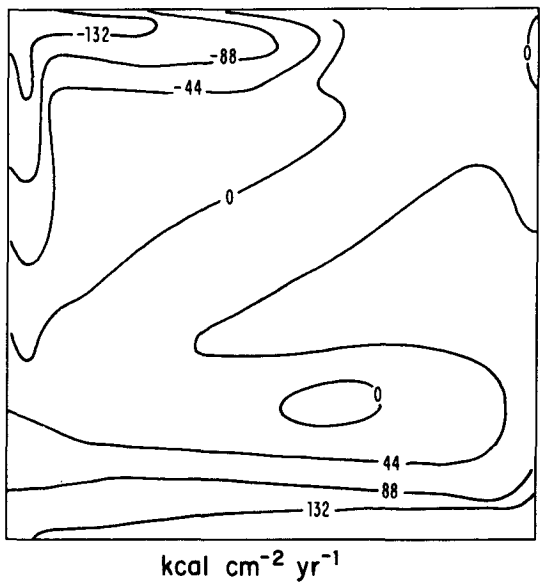

FIG. 17. Mean surface heat flux [Kcal cm^{-2} year^{-1} ($\sim$1.3 W m^{-2})]. See Bunker and Worthington (1976).

5) EFFECTS OF BOUNDARY PROCESSES ON MEAN BALANCES

Before leaving the mean balance of terms, we consider briefly the effects of the various model boundary condition parameterizations. The wind forcing is felt at O(1) in the u-momentum equation in the surface level. Bottom stress effects frequently dominate horizontal diffusive effects in the deep water, may be comparable to the leading ageostrophic terms in the NBC region, and play an O(1) role in the vertically integrated vorticity balance of the NBC(E). Surface heat flux effects are O(1) at the surface level in the mean heat equation and show strong cooling over the NBC region with maximum cooling (-180 kcal year^{-1} cm^{-2}); there is similarly strong heating near the southern boundary, and a small region of weak cooling about 500 km north of the southern boundary (See Fig. 17). Horizontal diffusion, due to the diffusive heat flux through the southern boundary, creates a boundary layer one grid space wide at the southern boundary.

5. Basin energy integrals

In order to explore the physical causes for the existence of the eddies and their maintenance against dissipation, and to investigate their role in the mean circulation, the overall energy integrals of the flow have been examined.

Using the basic model equations written in Cartesian tensor notation it is straightforward to derive the kinetic and potential energy equations for this system. Redefining p slightly, $p=\tilde{p}+\rho_0(1+\alpha T_0)gz$, so that

$$-\frac{1}{\rho_0}\frac{\partial}{\partial x_j}(u_j\tilde{p})=-\frac{1}{\rho_0}\frac{\partial}{\partial x_j}(u_jp)+(1+\alpha T_0)gw,$$

the kinetic energy equation is

$$\frac{\partial}{\partial t}(\tfrac{1}{2}u_\lambda u_\lambda)+\frac{\partial}{\partial x_j}(\tfrac{1}{2}u_j u_\lambda u_\lambda)=-\frac{1}{\rho_0}\frac{\partial}{\partial x_j}(u_j\bar{\bar{p}})+\alpha g w T + A_m u_\lambda\frac{\partial^2 u_\lambda}{\partial x_\delta \partial x_\delta}+K u_\lambda\frac{\partial^2 u_\lambda}{\partial z^2} \quad (5.1)$$

and the total potential energy equation

$$\frac{\partial}{\partial t}(-\alpha g z T)+\frac{\partial}{\partial x}(-\alpha g z T u_j)+\alpha g w T = -A_H\frac{\partial^2}{\partial x_\lambda \partial x_\lambda}(\alpha g z T)-K\alpha g z\frac{\partial^2 T}{\partial z^2}. \quad (5.2)$$

The summation convention of sum over the range of repeated subscripts is used with Latin subscripts ranging over 1, 2, 3 and Greek subscripts ranging over 1, 2.

From (5.1) and (5.2) we can derive the mean energy equations. The mean kinetic energy, $\frac{1}{2}(\overline{u^2+v^2})$, equals the sum of the kinetic energy of the mean flow (KEM), $\frac{1}{2}(\bar{u}^2+\bar{v}^2)$, plus the mean kinetic energy of the fluctuation flow, $\frac{1}{2}(\overline{u'^2}+\overline{v'^2})$. An equation for KEM comes from taking the dot product of $\bar{u}_\lambda$ with the mean momentum equations:

$$\bar{u}_\lambda\frac{\overline{\partial u_\lambda}}{\partial t}+\frac{\partial}{\partial x_j}(\tfrac{1}{2}\bar{u}_j\bar{u}_\lambda\bar{u}_\lambda+\bar{u}_j\bar{\bar{p}})+\bar{u}_\lambda\frac{\partial}{\partial x_j}\overline{u_j'u_\lambda'} = \bar{u}_\lambda A_m\frac{\partial^2\bar{u}_\lambda}{\partial x_\delta\partial x_\delta}+\bar{u}_\lambda K\frac{\partial^2\bar{u}_\lambda}{\partial z^2}+\alpha g\bar{w}\bar{T}. \quad (5.3)$$

The MKEF equation is obtained from subtracting (5.3) from the time mean of (5.1):

$$\frac{1}{2}\overline{\frac{\partial}{\partial t}u_\lambda'u_\lambda'}+\frac{\partial}{\partial x_j}(\tfrac{1}{2}\bar{u}_j\overline{u_\lambda'u_\lambda'}+\tfrac{1}{2}\overline{u_j'u_\lambda'u_\lambda'}+\overline{u_j'\bar{p}'})+\overline{u_j'u_\lambda'}\frac{\partial\bar{u}_\lambda}{\partial x_j} = \overline{u_\lambda' A_m\frac{\partial^2 u_\lambda'}{\partial x_\delta\partial x_\delta}}+\overline{u_\lambda' K\frac{\partial^2 u_\lambda'}{\partial z^2}}+\alpha g\overline{w'T'}. \quad (5.4)$$

The mean total potential energy equation (MTPE) is the time mean of (5.2), i.e.,

$$-\alpha g\left[\overline{\frac{\partial Tz}{\partial t}}+\frac{\partial}{\partial x_j}(\bar{u}_j\bar{T}z+\overline{u_j'T'z})\right] = -\alpha g\left[\bar{w}\bar{T}+\overline{w'T'}+A_H z\frac{\partial^2\bar{T}}{\partial x_\lambda\partial x_\lambda}+Kz\frac{\partial^2\bar{T}}{\partial z^2}\right]. \quad (5.5)$$

Note that terms like $\overline{\partial Tz/\partial t}$ and $\overline{(\partial/\partial t)u_\lambda'u_\lambda'}$ represent changes over the analysis record because of trends; by definition mean quantities are time independent.

Consider the basin integrated energy budgets using Eqs. (5.3), (5.4) and (5.5). A schematic of the energy flows in the basin integrated system is given in Fig. 18a and labels on the arrows indicate the process involved. The energy flow processes are derived from basin integrals of the terms of equations (5.3), (5.4) and (5.5)

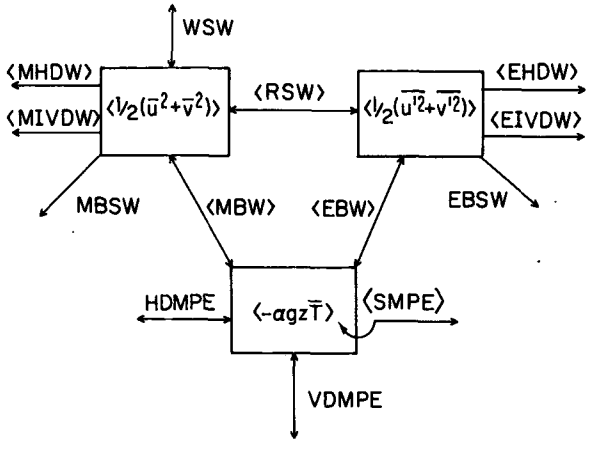

SCHEMATIC BASIN ENERGETICS

⟨ ⟩ indicates basin integrals
others are boundary terms

(a)

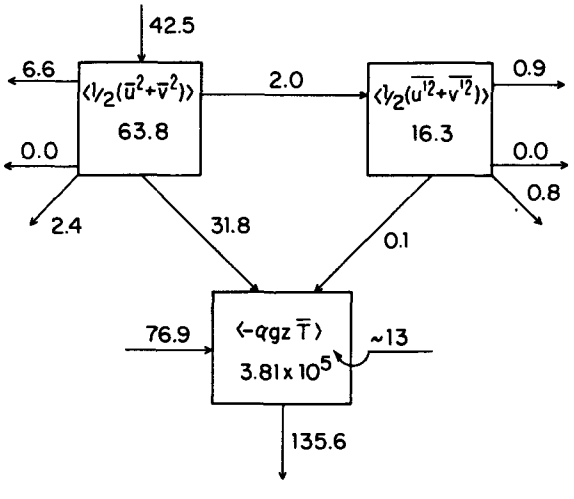

BASIN INTEGRATED ENERGETICS

Units: energy: erg cm⁻³
energy flux: erg sec⁻¹ cm⁻³ (x10⁻⁶)

(b)

FIG. 18. Basin energetics: (a) schematic energy flow for this system (see text) and (b) computed flows for this experiment.

and are defined as follows:

$\left\langle \overline{u_\lambda' u_j'} \frac{\partial \bar{u}_\lambda}{\partial x_j} \right\rangle = \langle \mathrm{RSW} \rangle$, the Reynolds stress work

$\langle \alpha g \bar{w} \bar{T} \rangle = \langle \mathrm{MBW} \rangle$, the buoyancy work of the mean

$\left\langle K \bar{u}_\lambda \frac{\partial^2 \bar{u}^k}{\partial z^2} \right\rangle = \mathrm{WSW} + \mathrm{BSW} + \langle \mathrm{MIVDW} \rangle$, the wind stress work, bottom stress work and work due to diffusion between the surface and bottom of the basin

$\left\langle A_m \bar{u}_\lambda \frac{\partial^2 \bar{u}_\lambda}{\partial x_\delta \partial x_\delta} \right\rangle = \langle \mathrm{MHDW} \rangle$, the work due to horizontal diffusion on the mean flow.

(The analogous terms for the MKEF are obtained from the above in the obvious way.)

$\left\langle -\alpha g z \frac{\overline{\partial T}}{\partial t} \right\rangle = \langle \mathrm{SMPE} \rangle$, the storage of mean potential energy

$\left\langle -\alpha g z A_H \frac{\partial^2 \bar{T}}{\partial x_\lambda \partial x_\lambda} \right\rangle = \mathrm{HDMPE}$, the horizontal diffusion of mean potential energy through the northern and southern boundaries

$\left\langle -\alpha g z K \frac{\partial^2 \bar{T}}{\partial z^2} \right\rangle = \mathrm{VDMPE}$, the diffusion of mean potential energy through the surface due to surface heat flux.

The angle braces signify integration over the entire basin.

The steady zonal wind driving is expected to be a source of KEM; horizontal diffusion work, internal vertical diffusion work and bottom stress work will all be sinks; Reynolds stress work and buoyancy work may be sources or sinks. The MKEF sources and sinks are just like those of KEM except there is no wind driving because the wind is steady. In principle there are also "storage" terms for KEM and MKEF due to the difference in these quantities between the beginning and end of the analysis record. They are found to be negligible and are not included in Fig. 18a, but it is necessary to retain $\overline{\partial T/\partial t}$. Mean and eddy buoyancy work transfer energy reversibly between KEM and MKEF, respectively, and MTPE; storage, horizontal diffusion and surface heating (cooling) will also affect MTPE. Fig. 18b shows the results of our experiment.

In the basin-integrated kinetic energy of the mean, we see that the largest work term is input by the wind. Seventy-five percent of this leaves as buoyancy work to maintain the thermal structure of the basin while 16% is lost to horizontal diffusive work, 5% to bottom stress work and 4% is converted into mean kinetic energy of the eddy field.

The MKEF system shows input from the KEM via Reynolds stress work to be the largest work term. Of this input, 45% leaves through horizontal diffusive work, 40% leaves through bottom stress work and 5% leaves as buoyancy work. This system is out of balance by about 8% because the eddy buoyancy work was computed from temperature data with the trend removed. The basin-averaged MKEF is approximately 25% of the basin-averaged KEM.

In the MTPE system the surface heat flux condition is removing potential energy from the system at three times the rate the wind is putting KEM in. Considerable input is observed from the north and south wall boundaries, and a smaller amount is stored over the course of the 618-day record. The 7% imbalance in the MTPE cannot be accounted for by the modification of basin eddy buoyancy work or storage due to the temperature trend, but cannot alter any conclusions drawn about the energetic properties of this system because of the balance observed in the MKEF and KEM systems.

From the energy diagrams we note that the flow is primarily wind driven rather than thermally driven. Of the internal transformations, the largest by over a factor of 15 is the mean buoyancy work which carries energy from the wind via mean currents to help maintain the mean thermal structure of the basin. The next most important adiabatic process is Reynolds stress work transfer of kinetic energy of the mean motion to mean kinetic energy of the fluctuations; thus the eddy field is maintained by a so-called barotropic instability process. Last in importance is the mean eddy buoyancy work which transfers a very small amount of energy per unit time from the MKEF to the MTPE. There is no net positive eddy buoyancy work (baroclinic instability) in our system. The remaining non-diffusive energetic term is the rate of storage of MTPE, which is about 40% of the mean buoyancy work and seven times the net Reynolds stress work. Even though the basin averaged temperature change over 618 days is only $\sim 0.01°C$, this thermal adjustment process involves considerable work. Horizontal diffusion work and bottom stress work are comparable in dissipating MKEF, but horizontal diffusion work does three times the work that bottom stress does on the KEM.

No calculation of available potential energy box diagrams for this flow has been made because of the relative insignificance of the eddy buoyancy work term. Examination of maps of mean eddy buoyancy work and Reynolds stress work reveals that baroclinic processes never do work greater than 10% of that of Reynolds stress processes in the region of largest generation of eddy energy, the eastern NBC(W)/Near Field. Whatever eddy available potential energy might be produced from mean available potential energy is diffused or dissipated rather than converted to eddy buoyancy work.

6. Discussion

The quasi-equilibrium circulation studied in our first wind and thermally driven high-resolution primitive equation experiment does include a spontaneously generated eddy field. The eddy space scales are somewhat larger than the first internal radius of deformation, and the time scales are on the order of those associated with related Rossby wave dispersion relationships as is the case in oceanic observations. The eddy energy is primarily in the barotropic mode, but about 10% is in the first baroclinic mode and some is in higher modes, but not systematically.

Dynamically distinct regions of the flow have been identified and their properties described. Balance of terms reveals that lateral momentum diffusion is never the dominant ageostrophic term in the momentum equations. This holds even in the boundary layers as we had hoped would be the case by our choice of r_N (Section 2a). Horizontal eddy effects can be the leading ageostrophic term in the interior mean momentum balance, but advection (horizontal and/or vertical) usually dominates eddy effects in intense current regions. Mean lateral momentum diffusion effects are generally less than or comparable to horizontal eddy effects throughout the Interior. The dominant instantaneous heat equation balance is advection/time change, with lateral diffusion typically 10% or less of the largest term. The dominant mean heat balance is advective-diffusive, but with horizontal eddy effects of order unity in the Near Field. The flow is quasi-geostrophic except in intense current regions where higher resolution would be of interest. Quasi-geostrophic potential vorticity is not conserved because diffusive processes cannot be neglected at order Rossby number in the heat equation.

Although the eddy flow amplitudes are considerably greater than the mean over the Interior of the flow, the linear Sverdrup relationship is seen to obtain for the mean transport to within the error limits imposed by the eddy variance and the length of this analysis record. In the NBC(W)/Near Field modification to the Sverdrup flow occurs through both mean advection and eddy flux divergence; in the WBC and NBC(E) the Sverdrup flow is modified dominantly by mean advection. In the southwest region eddy effects and mean advection contribute to the modification of the Sverdrup flow.

The existence of dynamically distinct regions requires compromises in the choice of modelling parameters and in fact many of the regional non-dimensional parameters are known only *a posteriori* in terms of the computed flow. Our choice of $\tau_0 = 4$ dyn cm^{-2} was made to favor inertial NBC effects. The nondimensional measure of eddy effects to the planetary vorticity flux divergence in the Sverdrup vorticity balance is $Cu'^2LH_1/l^2\tau_0$ where c is an eddy correlation coefficient and l an eddy length scale. Estimates of the ratio of this number for the North Atlantic to that in our model simulation are 10–30.

Basin energetic analysis shows that the eddy field is produced by Reynolds stress work that transfers energy from the kinetic energy of the mean flow (KEM) into the mean kinetic energy of the eddy flow (MKEF) at a rate of about 5% that at which the steady zonal wind adds energy to the mean flow. The small net eddy buoyancy work in the basin integral transfers energy out of MKEF into mean total potential energy (MTPE). Surface heat flux determined by the circulation decreases MTPE at three times the rate that the wind increases KEM. The diffusive temperature boundary conditions at the northern and southern boundaries increase MTPE at about twice the rate that the wind increases KEM. Oceanic values of horizontal heat fluxes are not known, but the surface heat flux over the NBC system is comparable to that given by Bunker and Worthington (1976) for the Gulf Stream, while the surface heat flux in the south shows stronger heating than described by Bunker and Worthington.

Examination of the regional contributions to the total Reynolds stress work terms shows that the dominant contribution occurs in the NBC(W)/Near Field region. Thus eddy energy is produced primarily in that region via a barotropic instability process. The relatively strong eddy energy in the Interior must be maintained by energy transferred primarily from this production region. It is interesting to note that a secondary production appears to occur via eddy buoyancy work in the southwest region, although the basin net integral of the buoyancy work term is negligible. Over the southwest region this baroclinic production seems to be about 10% of the total barotropic production in the NBC(W)/Near Field region.

The applicability of linearized instability theory to mean or instantaneous profiles is moot. However, consideration of the instability properties of the model flow indicates that our energetic results are not inconsistent with simple instability criteria. The classical necessary condition for shear instability of a barotropic zonal flow in a β-plane channel is $\partial^2\bar{u}/\partial y^2 = \beta$ somewhere. This condition is satisfied in the NBC(W) close to the separation and turning region and in some parts of the NBC(E); downstream in the NBC(W) $\partial^2\bar{u}/\partial y^2$ is uniformly smaller than β. For a westward flowing meridionally uniform zonal current in a two-layer model, only about 5 cm s^{-1} velocity difference across the layers is necessary for baroclinic instability. In the southwest where positive eddy buoyancy work is present the mean difference is $\sim$8 cm s^{-1}; it is somewhat larger for instantaneous values of the flow. In the eastward flowing NBC(E) there is sufficient vertical shear near the boundary to meet the pure baroclinic instability necessary condition of $\sim$30 cm s^{-1} change. However, Pedlosky's (1964) necessary criterion for the mixed instability of a two-layer zonal current with

vertical and lateral shear is only marginally met in the NBC(E). Where the NBC(W) satisfies the simple barotropic instability criterion, the modifications introduced by the mixed theory still lead to a prediction of instability.

It is of some interest to compare the results of our experiment with those of Holland and Lin (1975). The parameters of Table 1 are useful in considering which of the Holland and Lin simulations should be most nearly comparable to ours. Their study reveals many parameter-dependent differences in the model flows including the following: eddies are sometimes observed (cases 1, 3, 4, 7) but other flows are steady (cases 2, 5); when eddies are found they are often trapped near the NBC system (cases 1, 7) but sometimes they fill the basin (cases 3, 4); eddy buoyancy work can be the dominant energetic process for producing eddy energy (case 1) but Reynolds stress work transfer can be more important than eddy buoyancy work (cases 3, 4).

Holland and Lin suggest that r_W (the ratio of the frictional and inertial western boundary current widths) can be an important parameter in that two cases with identical r_W (cases 3, 4) had similar behavior. This parameter certainly cannot be always controlling because two other experiments with identical r_W (cases 1, 5) show different behavior from each other. Their results do suggest that in smaller r_W experiments (cases 3, 4 compared to case 1) the Reynolds stress work is of increasing importance relative to eddy buoyancy work in the overall energetics of the MKEF field. This trend is consistent with our finding that Reynolds stress work is responsible for the maintenance of the eddy flow in this experiment with r_W smaller than in any H&L case. The same trend is found using r_N instead of r_W.

Cases 3 and 4 are also most similar to our experiment in that they have an almost barotropic eddy field which fills the basin and a deep mean pressure field which is qualitatively similar in horizontal structure to the upper layer mean pressure. They also find that some aspects of the eddy field are similar to free basin modes, but their eddy fields resemble the (1,1) free basin mode while ours are more similar to the (1,3) mode (see Section 3d).

More detailed comparison is only possible with H&L case 1, for which H&L present the most complete discussion of any of their experiments. Unfortunately, this experiment is different from ours, in that the MKEF is produced primarily by eddy buoyancy work. However, several points of similarity can be found, among them that both have a ratio of basin integrated KEM to MKEF of $\sim$0.25, have similar vertically integrated vorticity balances in the WBC (when our vorticity terms are grouped together into H&L's terms), and have similarly complex NBC(W)/Near Field vorticity balances. Differences include the greater role of eddies and mean advection in the transport balance of the Interior and Southwest in our experiment and the O(1) role of the bottom stress curl (a process not present in H&L) in our NBC(E) vorticity balance.

Further experimentation in a parameter space including additional physical processes will be necessary before the relevance and importance of model results can be fully assessed. The comparison of model results with ocean data is just beginning. However, the results of this simulation, together with those of Holland and Lin (1975) and Semtner and Mintz (1977), indicate that the simulated eastward flowing Gulf Stream and its recirculation system effectively produce mesoscale eddy energy via mixed baroclinic and barotropic processes, which can be transported to populate a gyre. Whether or not this is the dominant process in the North Atlantic cannot be stated because of modeling simplification; but it must be considered as a probable operative process.

Acknowledgments. The numerical formulation and numerical calculation of the flow were carried out at UCLA; the analysis computations and interpretation were done primarily at Harvard. Drs. R. Haney and Y-J Han helped in the initial phases of the numerical formulation and flow computation. This work was supported by National Science Foundation Contract 1D076-00869 and Office of Naval Research Contract N00014-75-C-0025 to Harvard University and National Science Foundation Contract IDO 74-225-05 to UCLA. This is MODE Contribution 84 (POLYMODE).

REFERENCES

Bernstein, R. L., and W. B. White, 1974: Time and length scale of baroclinic eddies in the central North Pacific Ocean. *J. Phys. Oceanogr.*, **4**, 613–624.

Blandford, R. R. 1971: Boundary conditions in homogeneous ocean models. *Deep-Sea Res.*, **18**, 739–751.

Bretherton, F. P., and W. B. Owens, 1976: A numerical study of mid-ocean mesoscale eddies. Submitted to *Deep-Sea Res.*

Bryan, K., 1975: Three-dimensional models of the ocean circulation. *Numerical Models of Ocean Circulation*, National Academy of Science, Washington, D. C., 94–106.

——, and C. S. Cox, 1968: A nonlinear model of an ocean driven by wind and differential heating: Part I. Description of the three-dimensional velocity and density fields. *J. Atmos. Sci.*, **25**, 945–967.

Bunker, A. F., and L. V. Worthington, 1976: Energy exchange chars of the North Atlantic Ocean. *Bull. Amer. Meteor. Soc.*, **57**, 670–678.

Dantzler, L., 1977: Geographical variations in intensity of the North Atlantic and North Pacific eddy fields. *Deep-Sea Res.* (to appear).

Haney, R., 1971: Surface thermal boundary conditions for ocean circulation models. *J. Phys. Oceanogr.*, **1**, 241–248

——, 1974: A numerical study of the response of an idealized ocean of large-scale surface heat and momentum flux. *J. Phys. Oceanogr.*, **4**, 145–167.

Harrison, D. E., 1977: On eddy-mean field interaction in the ocean. Ph.D. dissertation, Harvard University.

Holland, W. R., and L. B. Lin, 1975: On the generation of mesoscale eddies and their contribution to the oceanic general circulation. *J. Phys. Oceanogr.*, **5**, 642–669.

Leith, C. E., 1973: The standard error of time-average estimates of climatic means. *J. Appl. Meteor.*, **12**, 1066–1069.

Lighthill, M. J. (1969): Dynamic response of the Indian Ocean to onset of the southwest monsoon. *Phil. Trans. Roy. Soc. London*, **A265**, 45–92.

McWilliams, J. C., 1976: Maps from the MODE experiment. Parts 1 and 2. *J. Phys. Oceanogr.*, **6**, 810–846.

——, and G. R. Flierl, 1976: Optimal, quasi-geostrophic wave analyses of MODE array data. *Deep-Sea Res.*, **23**, 285–300.

Pedlosky, J., 1964: The stability of currents in the atmosphere and the ocean: Part I. *J. Atmos. Phys.*, **21**, 201–219.

——, 1965: A study of the time dependent ocean circulation. *J. Atmos. Sci.*, **22**, 267–272.

Rhines, P. B., 1975: Waves and turbulence on a beta-plane. *J. Fluid Mech.*, **69**, 417–433.

——, 1976: The dynamics of unsteady currents. *The Sea*, Vol. 6, Goldberg *et al.*, Eds. (to appear).

Robinson, A. R. 1965: Oceanography. *Research Frontiers in Fluid Dynamics*, Seeger, R. J. and G. Temple, Eds., Interscience, Chap. 17.

——, 1975: The variability of ocean currents. *Rev. Geophys. Space Phys.*, **13**, 598–601.

Rooth, C. G., and H. Ostland, 1972: Penetration of tritium into the Atlantic thermocline. *Deep-Sea Res.*, **19**, 481–492.

Rossby, H. T., A. Voorhis, and D. Webb, 1975: A quasi-Lagrangian study of mid-ocean variability using long-range SOFAR floats. *J. Mar. Res.*, **33**, 355–382.

Schmitz, W. J., 1976: On the deep general circulation in the western North Atlantic. *J. Mar. Res.* (to appear).

Semtner, A. J., and Y. Mintz, 1977: Numerical simulation of the Gulf Stream and mid-ocean eddies. *J. Phys. Oceanogr.*, **7**, 208–230.

Veronis, G., 1966: Wind-driven ocean circulation—Part II. Numerical solutions of the non-linear problem. *Deep-Sea Res.*, **13**, 35–55.

Weatherly, G. L., 1972: A study of the bottom boundary layer of the Florida Current. *J. Phys. Oceanogr.*, **2**, 54–72.

Wyrtki, K., L. Maggard and J. Hager 1976: Eddy energy in the oceans. *J. Geophys. Res.*, **81**, 2641–2646.